Study of the energetic X-ray superflares from the active fast rotator AB doradus

Shweta Didel,[1]★ Jeewan C. Pandey [iD],[2]★ A. K. Srivastava [iD][1]★ and Gurpreet Singh[2]

[1]*Department of Physics, Indian Institute of Technology (BHU), Varanasi 221005, India*
[2]*Aryabhatta Research Institute of Observational Sciences (ARIES), Manora Peak, Nainital 2632001, India*

ABSTRACT

We present the analyses of intense X-ray flares detected on the active fast rotator AB Dor using observations from the *XMM–Newton*. A total of 21 flares are detected, and 13 flares are analysed in detail. The total X-ray energy of these flares is found to be in the range of 10^{34-36} erg, in which the peak flare flux increased up to 34 times from the pre-/post-flaring states for the strongest observed flare. The duration of these flaring events is found to be 0.7 to 5.8 h. The quiescent state X-ray spectra are found to be explained by a three-temperature plasma with average temperatures of 0.29, 0.95, and 1.9 keV, respectively. The temperatures, emission measures, and abundances are found to be varying during the flares. The peak flare temperature was found in the 31–89 MK range, whereas the peak emission measure was $10^{52.5-54.7}$ cm^{-3}. The abundances vary during the flares and increase by a factor of $\sim$3 from the quiescent value for the strongest detected flare. The variation in individual abundances follows the inverse-FIP effect in quiescent and flare phases. The X-ray light curves of AB Dor are found to exhibit rotational modulation. The semi-loop lengths of the flaring events are derived in the range of $10^{9.9-10.7}$ cm, whereas the minimum magnetic field to confine the plasma in the flaring loop is estimated between 200 and 700 G.

Key words: stars: abundances – stars: activity – stars: coronae – stars: flare – stars: individual: AB Dor – stars: magnetic field.

1 INTRODUCTION

The X-ray emissions from the late-type stars are well explained by the magnetic confinement of million-degree plasma residing in the coronal loops (see Reale 2014, and references therein). The magnetic field is supposed to be generated by the dynamo process working deep beneath the convective shells of the late-type stars. The presence of strong magnetic activities is indicated by the fact that strong X-ray emissions are observed even in their quiescent phase by the fast-rotating late-type stars, and the star spot covers large fractions of the stellar surface. Stellar coronae of these stars show a very dynamic nature of various activities, e.g. short explosive bursts of energy in time from a few minutes to several hours and slowly varying quiescent corona over a year to a few years. These short explosive bursts on stars are commonly known as flares. The magnetic reconnection process explains the energy released during the flares, which ranges from 10^{30-38} erg s^{-1} (Parker 1988; Benz & Güdel 2010). Since the stellar coronae are nearly 1000 times brighter than the Sun, the flares on stars are more energetic and impulsive than the Sun. The energetic flares having energy release $\geq 10^{33}$ erg s^{-1} are termed as superflares (Schaefer, King & Deliyannis 2000; Shibayama et al. 2013; Tsuboi et al. 2016; Pillitteri et al. 2022).

In the standard flares model, the magnetic reconnection process causes a rapid and transient catastrophic release of magnetic energy in the corona, leading to particle acceleration and electromagnetic radiation ranging from radio waves to γ-rays. These accelerated charged particles gyrate downwards along magnetic field lines, resulting in synchrotron radio emission. Hard X-rays are produced when these electron and proton beams collide with denser chromospheric materials. Simultaneous heating of the plasma to tens of millions of Kelvin evaporates cold material from the chromospheric footpoints, thus increasing the density of newly formed coronal loops and emitting UV and soft X-rays.

Stellar X-ray flares were extensively studied by several authors in the past (e.g. Pallavicini, Tagliaferri & Stella 1990; Getman et al. 2008; Pandey & Singh 2008, 2012). They come in various durations (ranging from a few minutes to a few hours), shapes, and sizes. van den Oord, Mewe & Brinkman (1988) found flares with short rise time as compact ones, while flares having longer rise time must be the two-ribbon flares. In some of the giant flares, double exponential decays are reported (see e.g. Favata & Schmitt 1999; Osten & Brown 1999; Favata et al. 2000). Superflares could also give information about the extent of coronae, e.g. if the flare is visible during a full rotation of a star, it means either the flaring region is very extended (Kuerster & Schmitt 1996) or the flare occurred near the pole (Maggio et al. 2000). Researchers have detected stellar superflares in optical and UV bands from a variety of sources, including RS CVn binaries, young T-Tauri stars, UV Ceti-like red dwarfs, and solar-like G-dwarfs (e.g. Haisch, Strong & Rodono 1991; Maehara et al. 2012; Kuznetsov & Kolotkov 2021). However,

★ E-mail: shwetadidel9@gmail.com (SD); jeewan@aries.res.in (JCP); asrivastava.app@itbhu.ac.in (AKS)

X-ray superflares have been observed in a few stars so far, e.g. Algol (Favata & Schmitt 1999), AB Dor (Maggio et al. 2000), II Peg (Osten et al. 2007), CC Eri (Karmakar et al. 2017), and SZ Psc (Karmakar et al. 2023).

Unlike Solar flares, stellar flares are spatially unresolved; however, a study of the complete evolution of a stellar flare can allow us to access information about the plasma structure and morphology. Coronal abundances are also found to be changing during the large flares (e.g. Tsuru et al. 1989; Stern et al. 1992; Pandey & Singh 2012; Karmakar et al. 2017), which suggest that flaring topologies can alter the fractionation processes in corona. This paper presents a detailed analysis of intense X-ray flares observed in the active star AB Dor A.

AB Dor A is a young, active, and a member of a pre-main-sequence quintuplet stellar system AB Doradus (= HD 36705) at a distance of 15.0 ± 0.1 pc (Guirado et al. 1997). The other companions, binaries AB Dor Ca/Cb (Climent et al. 2019) and AB Dor Ba/Bb (Vilhu & Linsky 1987) are faint sources and are ignored in the following work. Hereafter, we refer to AB Dor A as AB Dor throughout the text. AB Dor is a highly active ultrafast rotator of K0V spectral type with a rotational period of 0.5148 d (Pakull 1981). It shows frequent flaring activity, probably due to its high spin rate ($\sim$50 times that of the Sun). Therefore, it possesses a strong magnetic field. It has a radius (R_*) of $\sim$0.96 $R_\odot$, a mass of 0.86 $M_\odot$, and a surface temperature of 5081 K (see Guirado et al. 2011, and references therein). In the X-ray band, AB Dor has gained interest since its first detection by Einstein Observatory (Pakull 1981). AB Dor is observed by almost every X-ray satellite because of its X-ray brightness and positional advantage (galactic latitude $\sim -33°$). Kuerster et al. (1997) studied long-term X-ray activities using *ROSAT* data and found no significant trend throughout five years. Almost all X-ray observatories have detected frequent flares in the corona of AB Dor. Vilhu et al. (1993) first reported statistical studies of X-ray flares where they found mean flare energy of $\sim 10^{34}$ erg, putting AB Dor as a frequent superflaring star. In this context, we conducted a detailed study of X-ray flares on AB Dor using the *XMM–Newton* Observatory.

We organize the paper as follows. Section 2 gives the observations and the principle data reduction procedures. In Section 3, we have explained the analysis procedure in detail and showed the scientific results obtained from X-ray timing and spectral analysis. Finally, in Sections 4 and 5, we have discussed the results and presented our conclusion.

2 OBSERVATIONS AND DATA REDUCTION

AB Dor A was observed using the Reflection Grating Spectrometers (RGS; den Herder et al. 2001) and European Photon Imaging Cameras [EPIC; MOS (Turner et al. 2001) and PN (Strüder et al. 2001)] aboard the well-known *XMM–Newton* (Jansen et al. 2001). The EPIC cameras provide moderate spectral resolution (20–50 E/ΔE) and good angular resolution (6 arcsec PSF-FWHM) in the energy range of 0.1–15 keV. The RGS instruments offer substantially better spectral resolution (150–800) in the energy range of 0.33–2.5 keV (or 5–35 Å). The log of X-ray observations analysed in this paper is given in Table 1.

The Science Analysis System (SAS) software version 18.0.0 of *XMM–Newton* and the updated calibration files were used to perform the EPIC and RGS data reduction. The raw EPIC data were processed to generate the event files using the tasks EPPROC and EMPROC, respectively, for PN and MOS data. Due to the high background contribution at high energies, we have selected the energy range between 0.3 and 10.0 keV to analyse EPIC data. Further, to identify the high background proton flaring intervals from the event file, we used the task EVSELECT for energy greater than 10 keV. All the data

sets are found to be free from such intense proton flaring events. We also examined the pile-up effect data using the task EPATPLOT. It was significant for the observation of set S5, and a very little pile-up was present in the case of set S3. This pile-up effect was limited to the observation from PN CCD only. X-ray spectra and light curves from all EPIC observations were extracted from on-source counts obtained from circular regions around the source, whereas the background was chosen from source-free regions near the source in the same CCD. In order to avoid the pile-up effect for the observations S3 and S5, we chose annulus regions with inner and outer radii of 7.5 arcsec and 55 arcsec, and 20 arcsec and 68 arcsec, respectively. All the X-ray light curves obtained from EPIC observations were corrected for background contribution and other effects using task EPICLCCORR. Light curves from MOS1 and MOS2 detectors were added using LCMATH task. We used the ESPECGET task to create source and background spectra with redistribution matrix (RMF) and auxiliary (ARF) files. We then binned all the X-ray spectra to have a minimum of 20 counts per bin using the GRPPHA task.

The raw RGS data were reduced using the task RGSPROC to generate event files and other spectral products; however, tasks RGSLCCORR and RGCOMBINE were used to create RGS1 and RGS2 combined light curve and spectra, respectively. These grouped spectra were used for further analysis.

3 ANALYSIS AND RESULTS

3.1 X-ray light curves

The upper panels of Fig. 1 show the background-subtracted X-ray light curves of AB Dor as obtained from EPIC and RGS instruments in the energy range of 0.3–10 and 0.33–2.07 keV, respectively, whereas the lower panels show the variation of hardness ratio (HR) with time, which is defined as (H − S)/(H + S), where H is the count rate in the hard energy band of 2.0–10.0 keV and S is the count rate in the soft energy band of 0.3–2.0 keV.

The X-ray light curves of AB Dor also exhibit rotational modulations (e.g. Collier Cameron et al. 1988; Vilhu et al. 1993; Kuerster et al. 1997). Therefore, we used HR as a proxy to detect flaring events. We considered excursions greater than three times the standard deviation in the positive count rate from the pre-/post-flare light curves to identify flares. Flaring regions in the light curves were identified when HR increased and mimicked the flare light curve. Using this approach, we detected 21 flares during the observations used here. We marked all the identified flare durations as F*i* (where $i = 1, 2, ... 21$) in Fig. 1. Regions of constant HR beyond the flaring region of the light curves were identified as either pre- or post-flare epochs and were marked by P*i* (where $i = 1, 2, ... 11$) in the same figure. During the pre-/post-flare segments, HR remained almost constant. We fitted the following equation to model the light curve: the pre-/post-flare segments were fitted with a horizontal straight line, and the rise and decay phases of the flares were fitted with an exponential function.

$$c(t) = \begin{cases} c_0, & \text{for } t \leq t_0 \\ c_0 \exp(\frac{t-t_p}{\tau_r}), & \text{for } t_0 \leq t \leq t_p \\ c_0 \exp(-\frac{t-t_p}{\tau_d}), & \text{for } t \geq t_p \end{cases} \quad (1)$$

where c(t) is the time-dependent variation in count rate during the light curve, c_0 is the constant count rate during the quiescent state, t_0 and t_p denote the flare start time and flare peak time, respectively, and τ_r and τ_d are the e-folding rise and decay times of the flare.

In the case of sets S2, S3, S4, and S5, the rotational modulation appears to be present as both pre-flare and post-flare states were

Table 1. Log of observations of AB Dor with *XMM–Newton*.

Set	Observation ID	Instrument	Start time UTC	Exposure (s)	Offset (arcmin)	Src Radius (arcsec)	Bkg Radius (arcsec)	Mode	Filter
S1	0 123 720 301	PN	27/10/2000 15:23:55	55 700	0.145	70	50,50	Small window	Medium
		MOS	27/10/2000 15:10:06	56 049	0.145	110	110	Full frame	Medium
		RGS	27/10/2000 15:01:40	58 908	0.145	–	–	–	–
S2	0 134 520 701	PN	22/05/2001 17:05:58	48 220	0.145	70	50,50	Small window	Medium
		MOS	22/05/2001 16:50:15	49 019	0.145	80	80	Full frame	Medium
		RGS	22/05/2001 16:43:55	49 607	0.145	–	–	–	–
S3	0 412 580 701	PN	03/01/2011 02:10:27	10 000	0.009	7.5,55*	45,32	Small window	Thick
		MOS	03/01/2011 02:07:20	12 300	0.009	50	50	Small window	Thick
		RGS	02/01/2011 16:58:57	56 051	0.009	–	–	–	–
S4	0 412 580 801	PN	01/01/2012 02:09:42	10 001	0.009	65	46,46	Small window	Thick
		MOS	01/01/2012 02:06:59	9 999	0.009	48	48	Small window	Thick
		RGS	31/12/2011 15:41:48	60 770	0.009	–	–	–	–
S5	0 791 980 101	PN	07/10/2016 01:32:25	10 019	0.009	20,68*	45,45,25	Small window	Thick
		MOS	07/10/2016 01:26:56	10 077	0.009	54	54	Small window	Thick
		RGS	07/10/2016 01:26:47	98 313	0.009	–	–	–	–
S6	0 810 850 501	PN	30/09/2019 22:26:59	12 000	0.009	60	45,40	Small window	Thick
		MOS	30/09/2019 22:18:37	11 999	0.009	47	47	Small window	Thick
		RGS	30/09/2019 01:55:59	99 485	0.009	–	–	–	–

Note. *The selected region corresponds to the inner and outer radii of the annulus region used for pile-up removal.

observed at the different quiescent levels. Therefore, to account for the rotational modulation, we have fitted a sine wave with a period equal to the rotational period of AB Dor on the quiescent part of the light curve for sets S2, S4, and S5. However, in the case of set S3, we have fitted a sine wave with period half of the rotational period of AB Dor, which can occur due to the presence of two persistent active longitudes separated by $180°$ (e.g. Berdyugina & Usoskin 2003). After removing the rotational modulation from the original light curve, we applied the mentioned flare model fitting. Fig. 2 display the fitted sine wave, the original light curves, and the fitted flare model applied to the residual light curves. In the instance of set S1, we could not confirm the presence of rotational modulation, likely because the quiescent state was absent due to frequent flaring events occurring throughout the observation. Conversely, in the case of S6, significant rotational modulation was not detected.

We have used the data obtained from the PN detector to model the light curves for sets S1 and S2. However, RGS data were used for sets S3, S4, S5, and S6 because the PN detectors do not cover the entire observation for these sets. The best-fitting model parameters for all the 21 detected flares are shown in Table 2. The strength of these flares can be inferred from the quiescent to peak count rate ratio as mentioned in Table 2 by the parameter F/Q. The observed values of F/Q in AB Dor vary from ∼1.2 to ∼34, with most flares having F/Q of 2–4.

3.2 EPIC spectral analysis

In this section, we delve into an extensive discussion of the spectral analysis conducted on X-ray data from AB Dor, using observations from *XMM–Newton*. We employed time-resolved spectroscopy (TRS) to monitor changes in the X-ray spectral parameters throughout the observations. To begin, we isolated the flare components from the rest of the light curves. From the remaining light curve, we selected segments with the lowest mean count rates as pre- and/or post-flare segments, enabling us to identify the true quiescent state.

Our selection of 13 flares (F1-10, F13, F15, and F20 from RGS) out of the 21 total flares for TRS depended on the data available from the PN detector, which provided better statistics for low-exposure spectra. Furthermore, each flare was subdivided into multiple time bins, ensuring that each bin contained a similar and adequate number of counts for the subsequent spectral analysis.

3.2.1 The quiescent spectroscopy

We began by selecting the pre-/post-flare segments as proxies for the quiescent state in each observation and extracted the corresponding spectra. Fig. 3 showcases the quiescent state spectra of AB Dor from various observations. These X-ray spectra exhibited variations not only between different observations but also within a single observation. For instance, P3 and P4, both from the same observation, demonstrated inconsistency (refer also to Table 3).

To comprehend these variations, we conducted a comprehensive X-ray spectral analysis to determine parameters such as plasma temperature, emission measure, and abundance during these events. The quiescent state spectra were subjected to fitting with one (1-T), two (2-T), and three (3-T) temperature plasma models using APEC (Smith et al. 2001). We incorporated the X-ray absorption model PHABS to account for hydrogen column density (N_H), while solar photospheric abundances ($Z_{\odot}$) were adopted from Anders & Grevesse (1989). During spectral fitting, all temperatures, emission measures, and global abundances (Z) remained free parameters.

For N_H, we fixed it at the maximum value of Galactic N_H, which is 2×10^{18} cm^{-2} for AB Dor. This value of N_H was computed based on the maximum $E(B–V)$ value of 0.0003 mag for AB Dor (Boro Saikia et al. 2018) using the relation from Gorenstein (1975). The 3-T model exhibited a significantly better fit than the 1-T and 2-T models. The addition of another thermal component did not yield further improvement in the χ^2, and the parameters of the fourth component were not well constrained.

Table 3 summarizes the best-fitting model parameters along with their reduced χ^2 values for all the quiescent state spectra from P1 to P10. We calculated the average values of temperature (T_{QA}) and
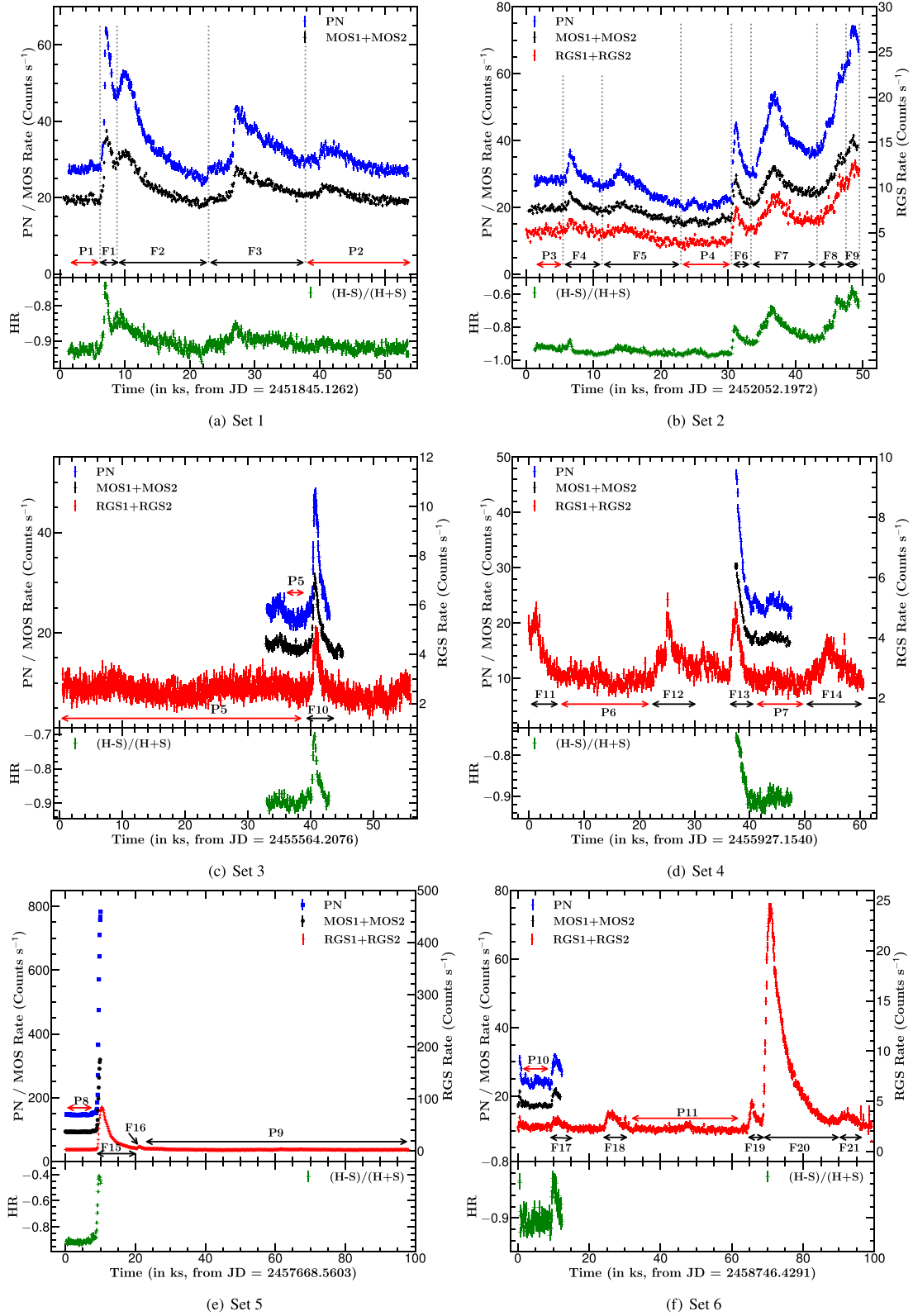
Figure 1. The background subtracted AB Dor's X-ray light curves for different observation epochs. The top, middle, and bottom light curves are from PN, MOS, and RGS detectors, respectively. In order to plot the light curves from all three detectors in the same panel, the MOS count rates are scaled up as $1.8 \times$ MOS for sets S1 and S2, 5+MOS for sets S3, S4, and S6, and 80+MOS for set S5. PN count rate is scaled up as $120 + $ PN for set S5 and RGS count rate is scaled up as $1.8 \times$ RGS for set S2.
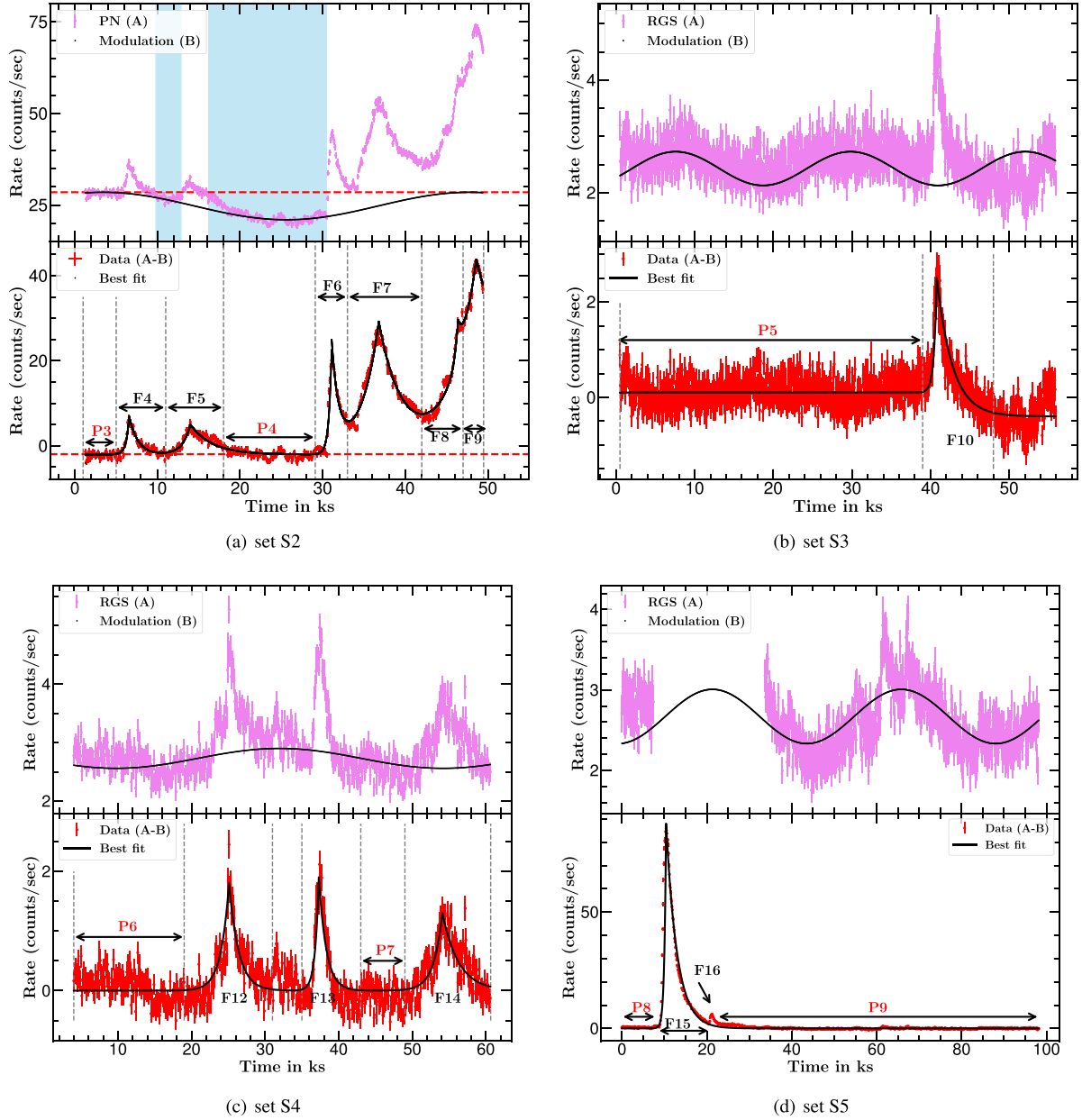
Figure 2. The upper panel displays the PN/RGS light curves for sets S2, S3, S4, and S5 (A), accompanied by the best fit sinusoidal curve (B). To show the rotational modulation in set S5, the flare part is not shown due to the very high count rate during this flare F15. The best-fitting flare model on the residual (A–B) is shown in the lower panel. The shaded regions in the upper panel of (a) represent the dimming areas as defined by Veronig et al. (2021), and the dotted lines show the level of pre-flare average counts.

emission measures (EM$_{QA}$) for each segment using the following formulas:

$$T_{QA} = \frac{\sum_{i=1}^{N} T_i EM_i}{\sum_{i=1}^{N} EM_i}; \quad EM_{QA} = \frac{1}{N} \sum_{i=1}^{N} EM_i, \quad (2)$$

where $N (= 3)$ represents the number of plasma components in the 3-T models. The calculated average values of T_{QA} and EM_{QA} were 0.94 ± 0.06 keV and $4.6 \pm 0.7 \times 10^{52}$ cm^{-3}, respectively. These average values exhibited consistency within a 2σ level (refer to Table 3). The X-ray luminosity (L_{XQ}) was found to be variable, indicating varying coronal active regions from one observation to another.

3.2.2 Spectral evolution during the flares

To trace the evolution of spectral parameters during flares, we divided the full flare light curve into several time segments consisting of the rising, peak, and decay phases and generated spectra for each segment. The rising, peak, and decay phases are denoted by Ri, P, and Di, respectively. Here $i = 1,2.....$ The length of each segment was chosen in such a way that each segment contained an equal number of counts. The TRS was conducted on all available flares using the PN detector due to its high signal-to-noise ratio. Additionally, TRS was performed for flare F20 due to high count rates in the RGS spectra.

Table 2. The best-fitting model parameters for all the detected flares. Here F/Q represents the ratio of the flare peak count rate to the quiescent count rate.

Parameters ($\rightarrow$) Segments ($\downarrow$)	τ_r (ks)	τ_d (ks)	F/Q	Parameters ($\rightarrow$) Segments ($\downarrow$)	τ_r (ks)	τ_d (ks)	F/Q
S1–F1	0.27 ± 0.01	3.01 ± 0.08	2.34 ± 0.04	F12	1.1 ± 0.1	1.3 ± 0.2	2.00 ± 0.09
F2	0.43 ± 0.06	3.7 ± 0.2	1.93 ± 0.03	F13	0.50 ± 0.05	1.02 ± 0.07	1.89 ± 0.09
F3	0.83 ± 0.04	6.7 ± 0.2	1.59 ± 0.03	F14	1.2 ± 0.2	2.9 ± 0.3	1.49 ± 0.08
S2–F4	0.35 ± 0.05	0.9 ± 0.1	1.30 ± 0.03	S5–F15	0.52 ± 0.02	2.19 ± 0.05	34.4 ± 0.4
F5	0.8 ± 0.1	2.2 ± 0.2	1.16 ± 0.03	F16	0.66 ± 0.06	0.92 ± 0.04	3.5 ± 0.1
F6	0.36 ± 0.02	0.84 ± 0.05	1.60 ± 0.03	S6–F17	0.8 ± 0.1	1.97 ± 0.20	1.53 ± 0.09
F7	2.19 ± 0.08	2.9 ± 0.1	2.56 ± 0.04	F18	0.84 ± 0.07	2.5 ± 0.2	1.79 ± 0.09
F8	0.42 ± 0.08	0.7 ± 0.2	2.84 ± 0.05	F19	0.51 ± 0.04	1.9 ± 0.1	2.3 ± 0.1
F9	2.99 ± 0.08	6.0 ± 1.0	3.50 ± 0.05	F20	0.96 ± 0.02	4.39 ± 0.06	11.0 ± 0.2
S3–F10	0.36 ± 0.05	1.09 ± 0.09	2.00 ± 0.05	F21	4.9 ± 0.9	2.4 ± 0.3	1.9 ± 0.1
S4–F11	2.9 ± 0.7	1.28 ± 0.09	1.89 ± 0.09	–	–	–	–
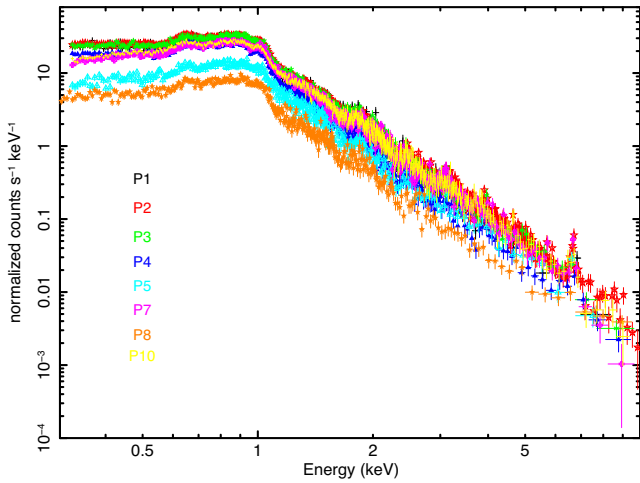
Figure 3. The X-ray spectra of pre- and post-flare states of AB Dor as obtained from EPIC-PN detector.

The maximum flare temperature T3 ranges from 2.7 to 3.8 keV for the rest of the flares. Also, we have found in the case of multiple flares (flares F1 and F2 from set S1 and flares F6 to F9 from set S2), the temperature during the decay phase of the flare is increasing rather than decreasing. This discrepancy can be attributed to the overlap between the decay phase of the first flare and the rising phase of the second flare. Within this overlapping region, the heating generated during the ascending phase of the second flare influences the cooling or decay phase of the preceding flare. Consequently, this overlapping effect leads to an overall increase in temperature. Further, the variation in emission measure EM3, abundance Z, and X-ray luminosity L_{XF} are found to be in agreement with the standard flare model and are shown in the second, third, and fourth plots of Figs 4(a) to (f). The values of peak EM3, Z, and L_{XF} were also found to be maximum for the flare F15 as 4.91×10^{54} cm^{-3}, 0.54 Z$_\odot$, and $>42.4 \times 10^{31}$ erg s^{-1}, respectively, whereas for the remaining flares the peak EM3, Z and L_{XF} were found to be in the range of $3.2 \times 10^{52} - 1.3 \times 10^{54}$ cm^{-3}, 0.22–0.33 Z$_\odot$, and 0.9–3.6 $\times 10^{31}$ erg s^{-1}, respectively.

The X-ray spectra of flaring segments were also fitted with 3-T APEC model. All the parameters of 3-T APEC model were kept free during the spectral fitting. The first two temperatures were found to be constant within a 1σ level and were similar to the quiescent temperatures. However, the third temperature was found to be varying during the flare. Therefore, for further spectral fitting, we have fixed the first two temperatures, and corresponding normalizations at the quiescent level and N_H at 2×10^{18} cm^{-2}. Other parameters like Z, the temperature of the third component, and the corresponding normalization were kept free.

We have also fitted the spectra with the 3 + 1-T APEC model, fixing all the parameters of the first three components to the nearest quiescent state value and varied parameters of the fourth component. This model either does not constrain the model parameter or does not improve the statistics of spectral fit. Therefore, we opted for the previous model for further analysis. All the best-fitting spectral parameters with 68 per cent confidence range and reduced χ^2 are given in Table A1 and temporal variation of all these parameters is shown in Fig. 4.

The top panels of Fig. 4 depict the temporal evolution of the third temperature T3, which shows that the flare temperature is maximum during the rising phase of the flare. The T3 reached a value of 7.7 keV during the flare F15, the highest of all the flares analysed here.

3.3 RGS spectral analysis

The RGS spectra were generated for both quiescent and flaring states and fitted with the 3-T VAPEC model along with the model PHABS to account for the N_H. For the quiescent states spectral fitting, the temperatures, and emission measures were kept free, whereas the N_H was fixed at 2×10^{18} cm^{-2}. However, the abundances of Al, and Ni were fixed to the solar photospheric values, while the remaining abundances were kept free and tied among each temperature component.

For the spectral fitting of the flaring states, we applied a similar approach as applied for the PN-spectral fitting. However, we used 3-T VAPEC model instead of the 3-T APEC model. We used the first two temperatures (kT1 and kT2) and emission measures (EM1 and EM2) as the proxy of the quiescent state. In order to achieve a sufficient signal-to-noise ratio, the flare in RGS requires stronger re-binning for spectral analysis than for the PN. Therefore, rather than dividing the flare into different segments as done for the PN spectral analysis, we used the spectra of the entire flaring event to determine the spectral parameters.

The best-fitting model parameters within a 68 per cent confidence range are given in Table A2 for both quiescent and flaring states of AB Dor. The best-fitting pre-flare P11 and flare F20 spectra with

Table 3. Best-fitting spectral parameters from the pre-/post-flare spectra using 3-T APEC model for all data sets.

Para ($\rightarrow$) Seg ($\downarrow$)	kT_1	kT_2	kT_3	T_{QA}	EM_1	EM_2	EM_3	EM_{QA}	Z ($Z_\odot$)	L_{XQ}	χ^2_ν (dof)
P1	$0.297^{+0.006}_{-0.006}$	$0.98^{+0.01}_{-0.01}$	$2.2^{+0.2}_{-0.2}$	$0.90^{+0.05}_{-0.04}$	$5.4^{+0.2}_{-0.2}$	$6.6^{+0.5}_{-0.5}$	$2.1^{+0.4}_{-0.3}$	$4.7^{+0.2}_{-0.2}$	$0.18^{+0.01}_{-0.01}$	$1.165^{+0.005}_{-0.005}$	1.27 (403)
P2	$0.288^{+0.003}_{-0.002}$	$0.974^{+0.006}_{-0.005}$	$1.99^{+0.04}_{-0.04}$	$1.0^{+0.01}_{-0.01}$	$4.8^{+0.1}_{-0.1}$	$6.3^{+0.2}_{-0.2}$	$3.6^{+0.1}_{-0.1}$	$4.90^{+0.08}_{-0.08}$	$0.194^{+0.005}_{-0.005}$	$1.277^{+0.002}_{-0.002}$	1.79 (742)
P3	$0.287^{+0.008}_{-0.007}$	$0.97^{+0.01}_{-0.01}$	$2.1^{+0.3}_{-0.1}$	$0.95^{+0.06}_{-0.04}$	$4.6^{+0.2}_{-0.2}$	$6.9^{+0.6}_{-0.4}$	$2.5^{+0.3}_{-0.4}$	$4.7^{+0.2}_{-0.2}$	$0.19^{+0.01}_{-0.01}$	$1.214^{+0.005}_{-0.005}$	1.03 (434)
P4	$0.282^{+0.007}_{-0.006}$	$0.94^{+0.02}_{-0.02}$	$1.8^{+0.2}_{-0.1}$	$0.85^{+0.05}_{-0.04}$	$3.7^{+0.2}_{-0.2}$	$4.0^{+0.4}_{-0.3}$	$1.8^{+0.3}_{-0.3}$	$3.2^{+0.2}_{-0.2}$	$0.20^{+0.02}_{-0.01}$	$0.863^{+0.004}_{-0.004}$	1.54 (361)
P5	$0.298^{+0.01}_{-0.008}$	$0.96^{+0.02}_{-0.02}$	$2.0^{+0.1}_{-0.1}$	$1.03^{+0.04}_{-0.04}$	$4.3^{+0.2}_{-0.3}$	$5.7^{+0.6}_{-0.5}$	$3.7^{+0.4}_{-0.4}$	$4.6^{+0.3}_{-0.2}$	$0.21^{+0.02}_{-0.02}$	$1.251^{+0.007}_{-0.007}$	1.07 (356)
P7	$0.278^{+0.005}_{-0.005}$	$0.86^{+0.02}_{-0.02}$	$1.5^{+0.1}_{-0.1}$	$0.97^{+0.05}_{-0.05}$	$3.5^{+0.2}_{-0.2}$	$3.6^{+0.3}_{-0.3}$	$5.3^{+0.3}_{-0.3}$	$4.1^{+0.2}_{-0.2}$	$0.23^{+0.02}_{-0.01}$	$1.07^{+0.01}_{-0.01}$	1.68 (523)
P8	$0.282^{+0.006}_{-0.007}$	$0.97^{+0.01}_{-0.01}$	$1.9^{+0.2}_{-0.1}$	$0.89^{+0.05}_{-0.03}$	$5.8^{+0.3}_{-0.3}$	$7.4^{+0.6}_{-0.6}$	$2.9^{+0.4}_{-0.4}$	$5.4^{+0.3}_{-0.3}$	$0.21^{+0.01}_{-0.01}$	$1.411^{+0.006}_{-0.006}$	1.29 (412)
P10	$0.270^{+0.004}_{-0.004}$	$0.952^{+0.008}_{-0.008}$	$1.9^{+0.1}_{-0.1}$	$0.91^{+0.03}_{-0.03}$	$5.9^{+0.2}_{-0.2}$	$6.9^{+0.3}_{-0.3}$	$3.6^{+0.2}_{-0.2}$	$5.5^{+0.1}_{-0.1}$	$0.18^{+0.01}_{-0.01}$	$1.346^{+0.004}_{-0.004}$	1.28 (546)
Avg	0.29 ± 0.01	0.95 ± 0.04	1.9 ± 0.2	0.94 ± 0.06	4.8 ± 0.9	6 ± 1	3 ± 1	4.6 ± 0.7	0.20 ± 0.02	1.200 ± 0.2	–

Note. The first row and first column represent the parameters (para) and light-curve segments (seg). All the temperatures and emission measures are in units of keV and 10^{52} cm^{-3}, respectively, whereas X-ray luminosity (L_{XQ}) is in units of 10^{30} erg s^{-1}. The error in the average values of the parameters in the last row is the standard deviation. The dof is the number of degrees of freedom, and χ^2_ν is the reduced χ^2.

the residual of the best-fitting 3-T VAPEC model are also illustrated in Fig. 5.

3.3.1 FIP and inverse FIP effect

The elemental abundances in the corona are not the same as those in the underlying photosphere because of the fractionation process related to the first ionization potential (FIP) of the elements. In slow rotators (e.g. Sun), generally, the so-called FIP effect is observed in which elements with FIP < 10 eV are enhanced relative to the elements with FIP > 10 eV (Feldman 1992; Laming, Drake & Widing 1995; Feldman & Laming 2000). However, it has been shown for a few fast rotating stars that the Inverse-FIP (I-FIP) effect occurs due to their higher magnetic activity (see Laming 2015, 2021). It has been observed that some stars do not show any FIP bias, which has been linked to their magnetically inactive chromospheres (Drake et al. 1994).

Fig. 6 shows the measured abundance as a function of FIP for the quiescent and flaring phases of different observations of AB Dor. The coronal abundances of elements Mg, Fe, and Si with FIP <10 eV, are found to be underabundant relative to solar photospheric values for both the quiescent and flaring states. The average abundance of Mg, Fe, and Si during quiescent states are found to be ∼0.31, ∼0.19, and ∼0.42, respectively. Also, all other high FIP elements except Ne (with an average abundance of ∼ 1.34) are found to be underabundant during quiescent states. Furthermore, our observations revealed the presence of the I-FIP effect during both quiescent and flaring states. In the majority of the flaring periods, the abundances of individual elements were observed to be higher compared to those in the quiescent state.

3.4 Loop modelling

Although stellar flares cannot be resolved spatially, their analogies with solar flares and loop models help us to infer the morphology and physical size of flaring loops and stellar corona. Observations of stellar flares do not always cover the entire duration of flares. In some cases, the rising phase is not covered, and in other cases, the decay phase is not observed. Also, in some flares, there is an overlap between the decaying phase of one flare and the rising phase of the other. In our case, only the decay phase of flare F13 and the rising phase of flare F15 are observed with the PN detector. So, the separate calculations for loop length from flare rise (Reale 2007) and decay

phases (Reale et al. 1997) have been made using the hydrodynamic loop model. This model assumes a single dominant coronal loop which includes plasma cooling as well as the heating effect during flare decay. We have determined the semi-loop length (L), using both of the approaches outlined below.

3.4.1 The rise phase

Reale (2007) introduced a detailed model for loop length calculation using the rise and peak phases of the stellar X-ray flare. As a consequence of the heating event, the loop's temperature experiences a rise, reaching its maximum at temperature T_0. Concurrently, due to chromospheric evaporation, the density also rises and peaks at temperature T_M within the flaring loop. During the peak phase, heating stops and conduction cooling starts to dominate, which causes the temperature to drop at the peak phase. At this stage, the continuous increase in density indicates the ongoing evaporation process.

Using hydrodynamic simulations of semicircular flaring loops with constant cross-section, Reale (2007) derived an empirical formula for semiloop length as

$$L_r = 950 \frac{T_0^{5/2}}{T_M^2} t_M \text{ cm}, \tag{3}$$

where L_r is the semiloop length in units of cm, T_0 and T_M are the maximum temperature and temperature at maximum density, respectively, in units of K, and t_M is the time at which density maximum occurs in units of s. The derived semiloop lengths using this model are given in Table 4 and were found to be in the range of 0.8–4.5×10^{10} cm. The largest loop length was found for flare F15, whereas the smallest loop length was found for flares F1, F6, and F9.

3.4.2 The decay phase

Considering pure cooling during the decay phase of the flare, Serio et al. (1991) derived single coronal loop length using thermodynamic cooling time-scales. Further, Sylwester et al. (1993) explained the sustained heating during the decay of spatially resolved solar flare by introducing the slope in the density–temperature diagram. In the process of explaining the slower decay, Reale et al. (1997) included the effect of significant heating during flare decay using a time-dependent hydrodynamic loop model and added a correction factor $F(\zeta)$ to the derived half loop length (L_d) as shown in the following equation.

(a) set S1

(b) set S2
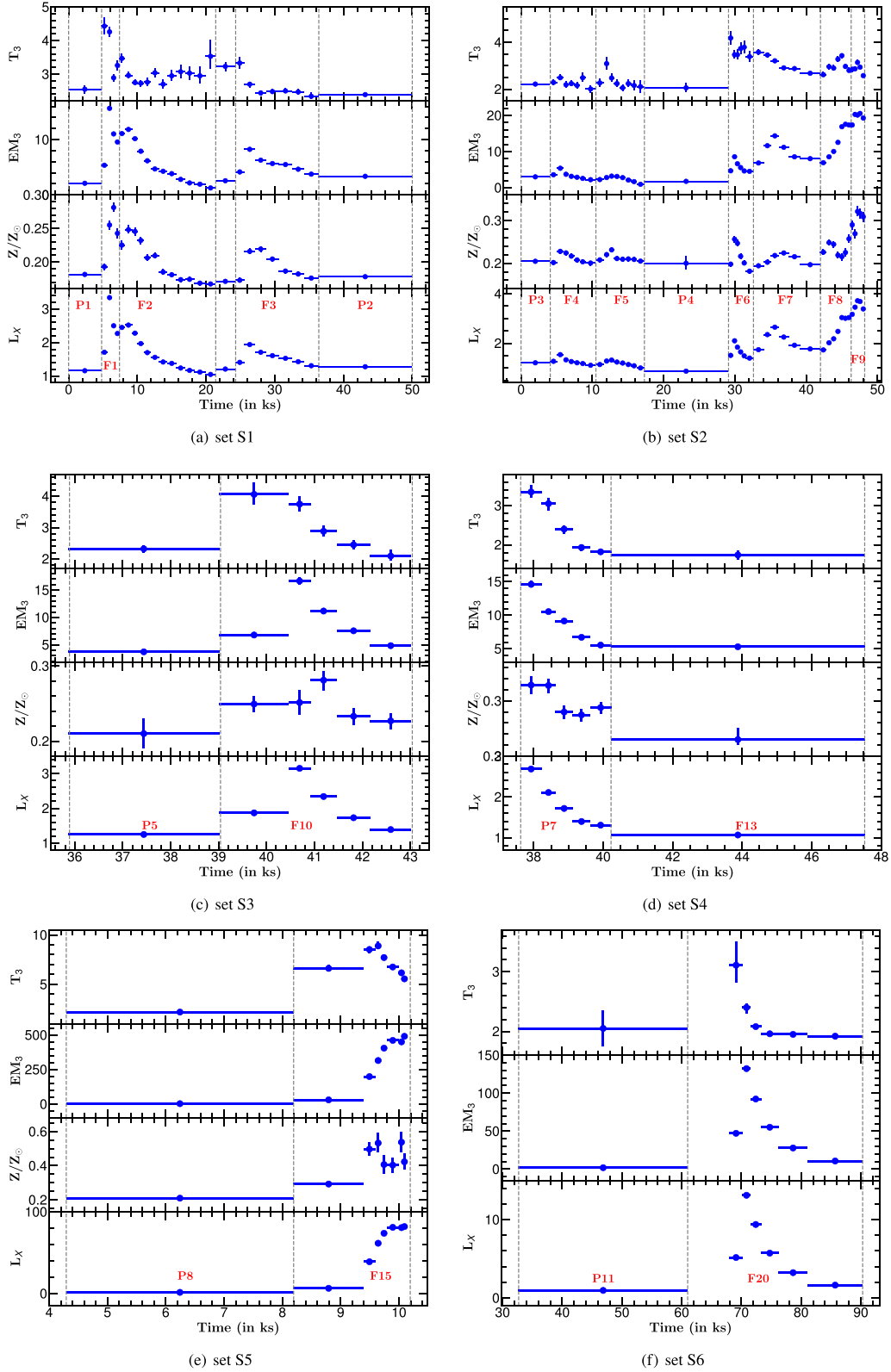
(c) set S3

(d) set S4

(e) set S5

(f) set S6

Figure 4. Temporal evolution of the spectral parameters of AB Dor during flares and quiescent states, where top to bottom plots show the variation of temperature (T_3) in units of 10^7 K, emission measure (EM_3) in units of 10^{52} cm^{-3}, relative abundance (Z/Z$_\odot$), and X-ray luminosity in units of 10^{30} erg s^{-1}.
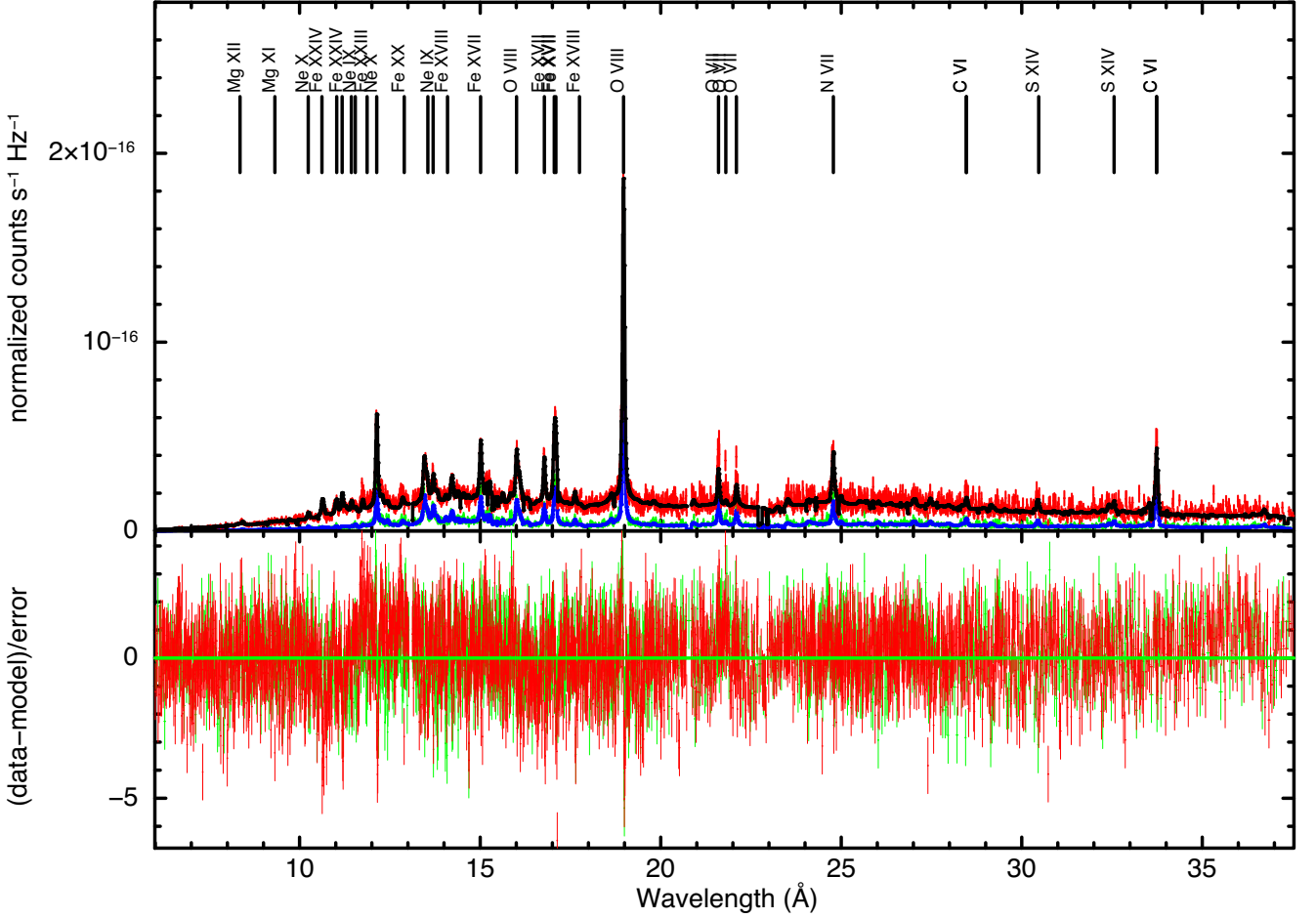
Figure 5. The upper curve represents the quiescent (P11) spectrum, while the lower curve corresponds to the flare (F20) spectrum for set S6. The best-fitting 3-temperature vapec model for both are shown with solid lines.

$$L_d = 2.7 \times 10^3 \frac{\tau_d T_{\max}^{1/2}}{F(\zeta)} \text{ cm} \quad \text{for} \quad 0.35 < \zeta \leq 1.6 \quad (4)$$

with $T_{\max} = 0.13 T_0^{1.16}$, $\quad F(\zeta) = \frac{0.51}{\zeta - 0.35} + 1.36 \quad (5)$

Here, ζ is the slope of the $\log(\sqrt{(\text{EM})})$ versus $\log(T)$ diagram (equivalent to density–temperature diagram) during the decay phase of the flare. This diagram is shown in Fig. 7 for the flares F7, F10, F13, and F20, along with the best-fitting straight line. The T_0 is the maximum best-fitting temperature derived from the spectral fitting of the data in units of K. The $F(\zeta)$ in equation (5) is valid for the observation from the EPIC instruments. A similar $F(\zeta)$ relation was adopted for observations from the RGS instrument (private communication with Reale F.). The slope (ζ) of the $\log(\sqrt{\text{EM}})$ versus $\log(T)$ curve is found to be 0.5 ± 0.1, 0.9 ± 0.1, 1.4 ± 0.2, and 0.21 ± 0.05 for flares F7, F10, F13, and F20, respectively. The low values of ζ indicate the presence of sustained heating during the decay of these flares. For the flare F20, the value of ζ is out of the range of the model. Therefore, loop length could not be derived from the decay method for F20. For the other flares where the decay phase was observed, we could not use this method as another flare emerged during the decay phase of the previous flare. This situation prevented us from tracing the density–temperature path, which is crucial for determining the loop length. The derived loop lengths for these flares are also given in Table 4. These values of the loop

lengths are well within 1σ with that derived from the flare rise method.

3.5 Loop parameters

We have calculated the flaring loop volume (V) using the approach used in the past in the absence of direct measurement (see e.g. Maggio et al. 2000; Pandey & Singh 2008) by using equation $V = 2\pi \beta^2 L^3$ cm³, where β is the ratio of loop radius to the half loop length. From the solar case, we assume the values of β between 0.1 and 0.3 (Golub et al. 1980). For $\beta = 0.3$, the V is estimated to be in the range of $3 \times 10^{29} - 5 \times 10^{31}$ cm³ and found to be maximum for flare F15 and minimum for flare F9. Using the values of V, $T_{\max}$, and peak emission measure (EM), we have derived the plasma density (n_e), pressure (p) at the loop apex, and minimum magnetic field ($B_{\min}$) required to confine the plasma inside the coronal loop. The total plasma density is a sum of electron and hydrogen ion densities (n_H). The n_H is found to be 0.8 times n_e.[1] Thus the values of n_e, p, V, and $B_{\min}$ are estimated as:

$$n_e = \sqrt{\frac{\text{EM}}{0.8V}} \text{ cm}^{-3}; \quad p = 1.8 n_e k T_{\max} \text{ dyne cm}^{-2}; \quad B_{\min} = \sqrt{8\pi p} \text{ G} \quad (6)$$

All the estimated values of V, n_e, p, and $B_{\min}$ are given in Table 4. The n_e was estimated in the range of 1 to 9×10^{11} cm⁻³, whereas the p was estimated to be in the range of 0.2 to 2×10^4 dyne cm⁻²

---

[1] As $n_{He} = 0.1 n_H$, hence $n_H/n_e = n_H/(n_H + 2n_{He}) = 1/1.2 = 0.833$

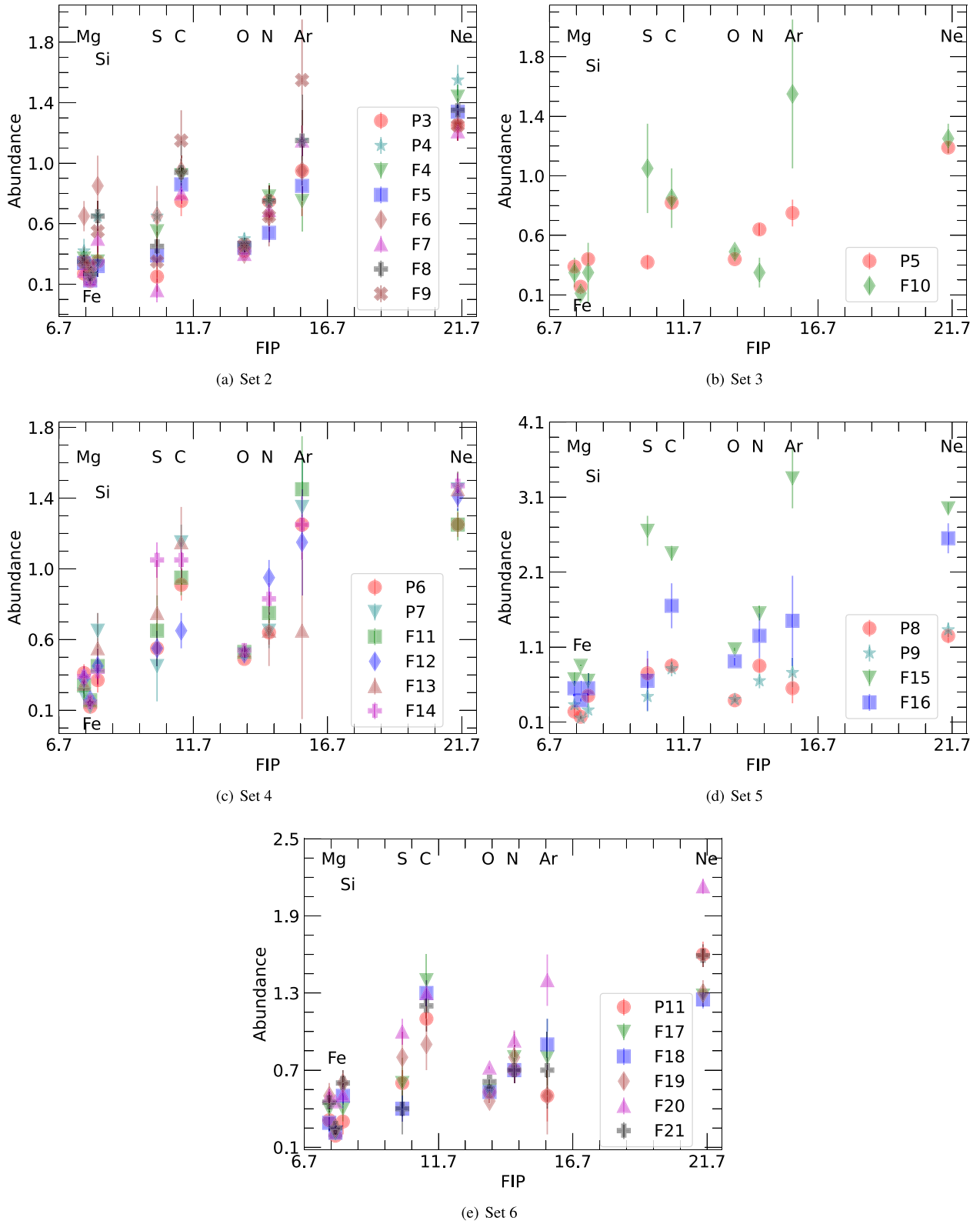**Figure 6.** Elemental abundances plotted as a function of FIP for both quiescent and flaring states during different observations of AB Dor.

for all the flares analysed here. The B_{min} was within the range of 200 to 700 Gauss. Among the flares studied, the parameters p and

B reached their highest values for flare F1, while the lowest values were observed for flare F5. In a scenario where β equals 0.1, these

Table 4. Loop parameters.

Flare (→) Parameters (↓)	F1	F2	F3	F4	F5	F6	F7
L_{XF} (10^{31} erg s^{-1})	0.982 ± 0.004	1.986 ± 0.004	1.094 ± 0.003	0.890 ± 0.003	0.941 ± 0.003	1.000 ± 0.004	1.268 ± 0.002
$E_{X, Total}$ (10^{34} erg)	3.20 ± 0.08	8.2 ± 0.4	8.2 ± 0.2	4.1 ± 0.3	4.4 ± 0.3	1.17 ± 0.06	7.0 ± 0.2
t_M (ks)	1.2	1.35	2.1	1.45	2.25	0.9	3.05
T_0 (MK)	44 ± 2	35 ± 1	33 ± 2	34 ± 1	31 ± 2	42 ± 3	36 ± 1
T_M (MK)	43 ± 2	30 ± 1	27 ± 1	25 ± 1	25 ± 2	35 ± 2	32 ± 1
L_r (10^{10} cm)	0.8 ± 0.1	1.0 ± 0.1	1.8 ± 0.2	1.5 ± 0.2	1.8 ± 0.4	0.8 ± 0.2	2.2 ± 0.2
L_d (10^{10} cm)	...	...	...	...	...	...	1.6 ± 0.7
V (10^{29} cm^3)	3 ± 1	6 ± 2	30 ± 13	21 ± 8	33 ± 22	3 ± 2	57 ± 16
n_e (10^{11} cm^{-3})	8 ± 1	5.1 ± 0.8	1.8 ± 0.4	1.8 ± 0.4	1.1 ± 0.4	6 ± 2	1.8 ± 0.2
p (10^4 dyne cm^{-2})	2.0 ± 0.4	0.9 ± 0.1	0.32 ± 0.07	0.32 ± 0.06	0.17 ± 0.06	1.4 ± 0.5	0.33 ± 0.05
B_{min} (G)	703 ± 69	481 ± 37	282 ± 31	285 ± 28	209 ± 36	584 ± 112	288 ± 21
B_{Total} (kG)	3.4 ± 0.6	1.9 ± 0.2	1.3 ± 0.2	1.3 ± 0.2	0.9 ± 0.2	1.9 ± 0.5	1.1 ± 0.1
E_{HR} (10^{31} erg s^{-1})	4 ± 1	1.8 ± 0.3	2.7 ± 0.7	2.8 ± 0.5	2.1 ± 0.8	3 ± 1	4.5 ± 0.7
$E_{H, Total}$ (10^{34} erg)	13 ± 3	8 ± 1	20 ± 5	13 ± 3	10 ± 4	4 ± 1	25 ± 4
M_{CME} (10^{18} g)	∼2.52	∼1.98	∼2.07	∼1.21	∼0.97	∼0.82	∼2.57
Flare (→)	F8	F9	F10	F13	F15	F20	–
L_{XF} (10^{31} erg s^{-1})	1.750 ± 0.005	1.743 ± 0.006	1.048 ± 0.006	>0.9[a]	>42.4[b]	3.62 ± 0.01	–
$E_{X, Total}$ (10^{34} erg)	2.0 ± 0.3	12 ± 2	1.5 ± 0.1	>1.4[a]	>115[b]	19.4 ± 0.3	–
t_M (ks)	3.55	1.3	1.675	...	1.95	2.85	–
T_0 (MK)	34 ± 1	31 ± 1	41 ± 4	34 ± 1	89 ± 4	31 ± 4	–
T_M (MK)	30 ± 1	29 ± 1	38 ± 2	34 ± 1	56 ± 2	24 ± 1	–
L_r (10^{10} cm)	2.6 ± 0.3	0.8 ± 0.1	1.2 ± 0.3	...	4.5 ± 0.5	2.5 ± 0.7	–
L_d (10^{10} cm)	...	...	1.2 ± 0.2	1.2 ± 0.1	...	...	–
V (10^{29} cm^3)	104 ± 35	2.9 ± 0.9	9 ± 7	10 ± 2	515 ± 172	88 ± 74	–
n_e (10^{11} cm^{-3})	1.5 ± 0.2	9 ± 1	5 ± 2	4.5 ± 0.6	3.4 ± 0.6	4 ± 2	–
p (10^4 dyne cm^{-2})	0.26 ± 0.05	1.5 ± 0.2	1.0 ± 0.4	0.8 ± 0.1	1.9 ± 0.3	0.7 ± 0.3	–
B_{min} (G)	255 ± 22	617 ± 48	504 ± 99	443 ± 29	682 ± 59	415 ± 91	–
B_{Total} (kG)	0.4 ± 0.1	2.5 ± 0.4	1.4 ± 0.4	1.0 ± 0.1	2.3 ± 0.3	0.8 ± 0.3	–
E_{HR} (10^{31} erg s^{-1})	4.7 ± 0.8	1.0 ± 0.2	4 ± 2	2.0 ± 0.3	379 ± 73	3 ± 2	–
$E_{H, Total}$ (10^{34} erg)	5 ± 1	7 ± 2	6 ± 3	3.0 ± 0.5	1027 ± 200	16 ± 8	–
M_{CME} (10^{18} g)	∼1.10	∼3.51	∼1.39	∼1.33	∼15.53	7.17	–

Notes. [a] Parameters derived using only the decay phase of the flare.
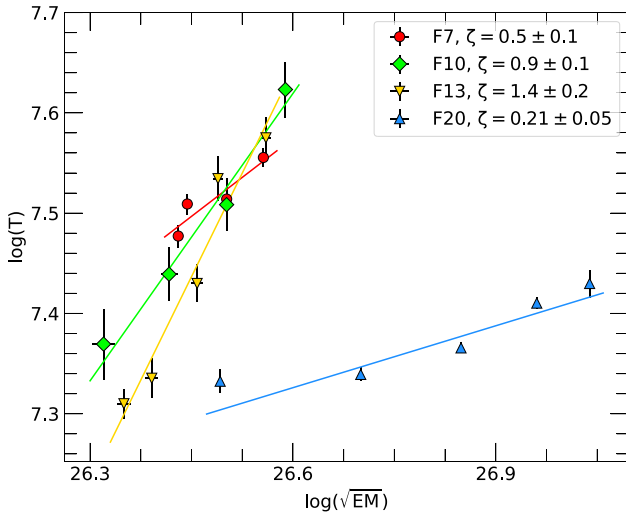[b] Parameters derived using only the rise phase of the flare.

Figure 7. Flare evolution in the log$\sqrt{EM}$ versus log(T) curve during the decay phase for flares F7, F10, F13, and F20 along with the best-fitting straight line. The slope (ζ) of the decay path of log$\sqrt{EM}$ versus log(T) is also given in the inset for each flare.

parameters would undergo transformations such that the V would become $\frac{V}{9}$, n_e would be $3n_e$, p would increase to $3p$, and B_{min} would change to $1.73B_{min}$.

The estimated loop lengths were found to be much smaller than the pressure scale height[2] of the flaring plasma of AB Dor. Therefore, one can assume that the flaring loops are close to a steady-state condition. Thus, the RTV scaling law (Rosner, Tucker & Vaiana 1978) can be applied for the estimation of the physical parameters of flaring plasma (see also Aschwanden, Stern & Güdel 2008).

The heating rate per unit volume (HR_V) at the flare peak can be estimated by the following RTV relationship:

$$HR_V \sim 10^{-6} T_{max}^{7/2} L^{-2}. \tag{7}$$

Assuming the constant heating during the rise and decay phases of the flare, the total heating rate (E_{HR}) can be estimated as ($E_{HR} \sim HR_V \times V$). The total energy corresponding to the heating rate is calculated as $E_{H, Total} = E_{HR} \times (\tau_r + \tau_d)$. The estimated values E_{HR} and $E_{H, Total}$ are found to be in the range of $1 \times 10^{31} – 4 \times 10^{33}$ erg s^{-1}, and $3 \times 10^{34} – 1 \times 10^{37}$ erg, respectively. These parameters were found to be maximum for the strongest flare F15 observed in the sample.

[2]$h_p = kT_{max}/\mu m_H g$, where k is Boltzmann's Constant, T_{max} is the maximum temperature, μ is mean molecular weight, m_H is the mass of a hydrogen atom, and g is surface gravity of the star.

Under the assumption that the energy released during a flare is of magnetic origin, we have calculated the total non-potential magnetic field (B_{Total}) within the active region of the star that corresponds to the release of flare energy. The B_{Total} is found to be in the range of 0.4 to 3.4 kG, as determined by the equation $E_{H,\text{Total}} = (B_{\text{Total}}^2 - B_{\text{min}}^2) \times V/8\pi$. For a comprehensive overview of all estimated loop parameters for AB Dor, please refer to Table 4.

4 DISCUSSION

The quiescent level always exists in the stars even during the flare, so, confining quiescent emission becomes much more important in studies of flares. We found that the quiescent corona of AB Dor can be well described by three temperature plasma models. In this study, the average values of T_{QA} and EM_{QA} are found to be 0.94 keV and 4.6×10^{52} cm^{-3} from APEC model, and 1.1 keV and 3.1×10^{52} cm^{-3} from VAPEC model, respectively. These values of T_{QA} and EM_{QA} are consistent with those from the earlier studies of AB Dor (e.g. Güdel et al. 2001; Sanz-Forcada, Maggio & Micela 2003). The quiescent state luminosity, L_{XQ} of AB Dor is not found to be constant for different observations analysed here. It was found to be highest during P8 with a value of 1.4×10^{30} erg s^{-1} whereas, during P4, the value of L_{XQ} of 0.9×10^{30} erg s^{-1} is found to be lowest.

We have performed a comprehensive study of the 13 strongest X-ray superflares out of a total of 21 observed flares on AB Dor using a large set of data sets from 2000 to 2019 with the *XMM–Newton* satellite. The time duration of these 21 flares ranges from ∼0.7 to ∼5.8 h. The e-folding rise and decay times of these flares are found to be in the range of 0.27–4.9 and 0.7–6.7 ks, respectively, which shows the rapid rise and slower decay pattern of the flares. This kind of trend has been found in many solar and stellar flares (van den Oord, Mewe & Brinkman 1988; Pandey & Singh 2008, 2012; Yan et al. 2021). Similar to the flares observed in the past, the F/Q ratios of the flares observed are in the range of 2–4 (e.g. Güdel et al. 2001; Lalitha & Schmitt 2013). In this study, flares F15 and F20 have the highest values of F/Q of 34 and 11, respectively. Earlier two strongest X-ray flares were observed in 1997 by BeppoSAX with F/Q of ∼100 (Maggio et al. 2000). These two X-ray flares from BeppoSAX appear to be the strongest flares observed thus far and in our present data the flares F15 and F20, appear to be the next two strongest flares observed in AB Dor thus far.

The detailed TRS analysis shows the variation in spectral parameters during the flaring events. The peak flare temperature was found to be in the range of 31 to 89 MK. Flares F5, F9, and F20 had the lowest peak temperatures, while flare F15 had the highest, and were ∼3 to 8 times higher than the quiescent temperature. Whereas, the peak emission measure was found to be in the range of 3.2×10^{52} to 4.9×10^{54} cm^{-3} in which the maximum value is found for flare F15. Based on the results of TRS, it has been observed that the flare temperature peaks during the rising phase while the emission measure peaks during the peak phase of the flare. This type of delay between peak temperature and peak emission measure has been also found in many solar and stellar flares (van den Oord & Mewe 1989; Sylwester et al. 1993; Stelzer et al. 2002). The reason behind this delay is the possible magnetic reconnection process, which leads to the particle acceleration and chromospheric evaporation process (Reale 2007). The temporal variation in flare temperature of independent single flares and multiple overlapped flares is found to be different. In the case of independent single flares, the temperature rises during the flare's rising phase and decreases during the decay phase due to conduction and radiative cooling.

However, in multiple overlapped flares, the temperature remains either constant or increases during the decay phase, as the decay phase of one flare is overlapped with the rising phase of the next flare.

We have also traced the global coronal abundances during the flaring events and found them to be varying as the flare evolves. It is found to be peaked around the peak phase of the flare. We found a 1.1 to 2.7-fold increase in abundances from the quiescent state value (∼0.2 $Z_\odot$) with a maximum increase in abundances for the strongest flare F15. The enhancement in the coronal abundance during the flares could be related to an increase in density within the flaring loop of constant volume which is indicative of a large amount of evaporation of chromospheric material inside the loop due to intense heating during the flares.

The elemental coronal abundances add extra information to the physical nature of the corona of AB Dor. The abundance of the majority of elements was found to be underabundant during the quiescent with respect to the solar photospheric values. However, the abundance of Ne in the quiescent state was found to be more than the solar photospheric value. As the solar photospheric Ne abundances are much uncertain due to the lack of photospheric absorption lines, so, Ne is usually quoted with reference to some other high FIP elements like oxygen, whose photospheric values are well constrained. Here, by assuming the photospheric values of AB Dor similar to the solar photospheric values (Wood et al. 2018), we noticed during the flares (Ne/O)$_*$ ratio ranges from 0.34 to 0.52, whereas the average quiescent value is 0.44 with a minimum of 0.39 and a maximum of 0.48, which is similar to the values reported by Drake & Testa (2005) for the active stars. Although the FIP effect observed with this assumption was challenged in some cases (studied in detail by Sanz-Forcada, Favata & Micela 2004). In contrast to solar corona where low FIP elements show enhanced abundances with respect to high FIP elements (von Steiger et al. 1995; Feldman & Laming 2000; Laming 2015), the corona of AB Dor shows inverse FIP effect. Such inverse FIP effect is found in active M dwarfs and active binaries (Liefke et al. 2008) and also has been reported for AB Dor by many authors in the past (Maggio et al. 2000; Güdel et al. 2001; Lalitha et al. 2013). An inverse-FIP effect near sunspots during flares has recently been detected for the first time (Doschek, Warren & Feldman 2015), which supports that the highly active region shows the I-FIP phenomenon. The Solar-like FIP effects at older aged stars are noticed whereas an inverse-FIP or no FIP effect has been found for the younger (<300 Myr) and most active stars (Telleschi et al. 2005). Further, it has been reported that there is a strong relationship between spectral class and FIP bias, with M dwarfs having an inverse-FIP effect that decreases to zero at a mid-K spectral type and subsequently drifts towards a solar-like FIP effect for early G dwarfs (Wood & Linsky 2010; Wood, Laming & Karovska 2012). As AB Dor is a young and highly active K dwarf, therefore, the I-FIP effect is expected. The Fe/O ratio can be used as a proxy to the extent of FIP bias in coronal abundances (Wood & Linsky 2010). We found the (Fe/O)$_*$ abundance during the quiescent state ranges from 0.02 to 0.03. The smaller value for the Fe/O abundance is indicative of a stronger I-FIP effect. The quiescent corona of AB Dor showed the I-FIP effect at nearly the same level for the time-span of 19 yrs, which is longer than the photospheric activity cycle of AB Dor (see Güdel et al. 2001). It appears as if the fractionation process that is causing FIP bias in AB Dor is independent of the magnetic activity cycle of AB Dor. Furthermore, the I-FIP effect seems to remain the same or get weaker during the flaring epochs with (Fe/O)$_*$ abundance in the range of 0.02–0.04. For the strongest flare F15 in the current sample, the (Fe/O)$_*$ ratio is found to be a

maximum of 0.04, indicating a weaker inverse FIP effect, whereas the overall abundances of each element increase during the flares due to the filling of dense plasma from chromospheric footpoints. One of the possibilities is that the weakened inverse FIP effect is a result of a higher heating rate compared to magnetic energy, which, in turn, weakens the fractionation process. Although the precise physical mechanisms for the FIP effect are still not fully understood, it is suspected that the drivers of this effect are the Alfven wave heating of the corona and the associated ponderomotive force (Laming 2004, 2021).

Using the hydrodynamic loop model, we have derived the semiloop length of the flares and found it to be in the range of 0.8–4.5×10^{10} cm. The estimated loop length is also found to be similar to the earlier observed flares on AB Dor (Güdel et al. 2001; Mason et al. 2001; Hussain et al. 2007; Lalitha et al. 2013). The highest loop length in AB Dor was found to be $\sim 8.8 \times 10^{10}$ cm in 2009 November observations (Lalitha et al. 2013). In the case of the Sun, the typical loop length is found to be of the order of 10^{9}–10^{10} cm (Mullan 2009). The loop heights ($2L/\pi$) corresponding to semiloop lengths of all these flaring events observed so far are 8 to 43 per cent of the radius of AB Dor. The total energy released by the flares was estimated to be in the range of 3×10^{34}–1×10^{37} erg, which is very large in comparison to the total energy of the strongest flares observed on the Sun ($\sim 10^{32}$ erg; Emslie et al. 2012; Zimovets, Sharykin & Gan 2020). Also, the total magnetic field of the loop is found to be around 0.4–3.4 kG, which is the typical magnetic field observed in AB Dor (Donati & Collier Cameron 1997; Jardine et al. 1999).

If we closely inspect the PN light curve of the post-flare phase of set S2, we notice a continuous dimming as shown by Veronig et al. (2021). A rotational modulation appears in most X-ray light curves of AB Dor, possibly due to the stellar surface's eclipsing of the coronal active regions (Singh et al., private communication). After removing the effect of rotational modulation from set S2 and following the definition of dimming as given in Veronig et al. (2021), we did not see any strong signature of such dimming in the light curve (see Fig. 2). An empirical relationship between the stellar flare energy in X-rays and its associated CME mass is estimated as $M_{\mathrm{CME}}(g) = 10^{-1.5 \pm 0.5} E_G^{0.59 \pm 0.02}$, where E_G is the X-ray energy in GOES (1–8 Å) energy band (Aarnio, Matt & Stassun 2012; Drake et al. 2013). The derived X-ray flux is converted into GOES flux using WEBPIMMS for the derived flare temperatures of AB Dor as described in Section 3.2.2. The estimated values of M_{CME} for AB Dor are found to be in the range 10^{18-19} g and found to be maximum for the flare F15. These values of CMEs are 10 to 100 times more than the most massive solar CME (Yashiro & Gopalswamy 2009) and similar to other stellar CMEs (Gunn et al. 1994; Namekata et al. 2021; Karmakar et al. 2022).

5 SUMMARY AND CONCLUSIONS

We have analysed quiescent and flaring X-ray emission of the active fast rotating star, AB Dor. In most of the observations, we observed rotational modulation in the quiescent state light curves. The quiescent state of AB Dor consists of three temperature plasma with an average value of the temperature, emission measure, and abundances of 0.94 keV, 4.6×10^{52} cm^{-3}, and 0.2 Z$_\odot$, respectively. The quiescent state luminosity of AB Dor was not found to be constant over the 19 yr of observations supporting the presence of long-term variations. A total of 21 flares are detected from six observations of AB Dor with a flare-to-quiescent state count rate ratio of 2–4 for the majority of flares. The most powerful flares

observed in AB Dor are identified as F15 and F20, with flare-to-quiescent state count rate ratios of 34 and 11, respectively. The flare F15, which occurred in 2016, emerges as the third most powerful flare following the two strongest flares documented during the BeppoSAX observations in 1997. The most intense flare, F15, exhibits a peak temperature of 89 MK, unlike the other flares, which all have peak temperatures below 50 MK. In most flares, we observe an increase in abundance and density, suggesting chromospheric evaporation. The elemental abundances exhibit an inverse FIP bias in both quiescent and flaring conditions. The heights of the loops in these flares do not extend beyond 50 per cent of the stellar radius. Additionally, the erupted mass of CMEs appears to be 10 to 100 times higher than the most massive solar CME.

DATA AVAILABILITY

The XMM–Newton data used for analysis in this article are publicly available in NASA's High Energy Astrophysics Science Archive Research Center (HEASARC) archive (https://heasarc.gsfc.nasa.gov/docs/archive.html).

REFERENCES

Aarnio A. N., Matt S. P., Stassun K. G., 2012, ApJ, 760, 9
Anders E., Grevesse N., 1989, Geochim. Cosmochim. Acta, 53, 197
Aschwanden M. J., Stern R. A., Güdel M., 2008, ApJ, 672, 659
Benz A. O., Güdel M., 2010, ARA&A, 48, 241
Berdyugina S. V., Usoskin I. G., 2003, A&A, 405, 1121
Boro Saikia S. et al., 2018, A&A, 616, A108
Climent J. B., Berger J. P., Guirado J. C., Marcaide J. M., Martí-Vidal I., Mérand A., Tognelli E., Wittkowski M., 2019, ApJ, 886, L9
Collier Cameron A., Bedford D. K., Rucinski S. M., Vilhu O., White N. E., 1988, MNRAS, 231, 131
den Herder J. W. et al., 2001, A&A, 365, L7
Donati J. F., Collier Cameron A., 1997, MNRAS, 291, 1
Doschek G. A., Warren H. P., Feldman U., 2015, ApJ, 808, L7
Drake J. J., Testa P., 2005, Nature, 436, 525
Drake J. J., Laming J. M., Widing K. G., Schmitt J. H. M. M., Haisch B., Bowyer S., 1994, in American Astronomical Society Meeting Abstracts #184, 05.22
Drake J. J., Cohen O., Yashiro S., Gopalswamy N., 2013, ApJ, 764, 170
Emslie A. G. et al., 2012, ApJ, 759, 71
Favata F., Schmitt J. H. M. M., 1999, A&A, 350, 900
Favata F., Reale F., Micela G., Sciortino S., Maggio A., Matsumoto H., 2000, A&A, 353, 987
Feldman U., 1992, Phys. Scr., 46, 202
Feldman U., Laming J. M., 2000, Phys. Scr., 61, 222
Getman K. V., Feigelson E. D., Broos P. S., Micela G., Garmire G. P., 2008, ApJ, 688, 418
Golub L., Maxson C., Rosner R., Vaiana G. S., Serio S., 1980, ApJ, 238, 343
Gorenstein P., 1975, ApJ, 198, 95
Güdel M. et al., 2001, A&A, 365, L336

Guirado J. C. et al., 1997, ApJ, 490, 835

Guirado J. C., Marcaide J. M., Martí-Vidal I., Le Bouquin J. B., Close L. M., Cotton W. D., Montalbán J., 2011, A&A, 533, A106

Gunn A. G., Doyle J. G., Mathioudakis M., Houdebine E. R., Avgoloupis S., 1994, A&A, 285, 489

Haisch B., Strong K. T., Rodono M., 1991, ARA&A, 29, 275

Hussain G. A. J. et al., 2007, MNRAS, 377, 1488

Jansen F. et al., 2001, A&A, 365, L1

Jardine M., Barnes J. R., Donati J.-F., Collier Cameron A., 1999, MNRAS, 305, L35

Karmakar S., Pandey J. C., Airapetian V. S., Misra K., 2017, ApJ, 840, 102

Karmakar S., Naik S., Pandey J. C., Savanov I. S., 2022, MNRAS, 509, 3247

Karmakar S., Naik S., Pandey J. C., Savanov I. S., 2023, MNRAS, 518, 900

Kuerster M., Schmitt J. H. M. M., 1996, A&A, 311, 211

Kuerster M., Schmitt J. H. M. M., Cutispoto G., Dennerl K., 1997, A&A, 320, 831

Kuznetsov A. A., Kolotkov D. Y., 2021, ApJ, 912, 81

Lalitha S., Schmitt J. H. M. M., 2013, A&A, 559, A119

Lalitha S., Fuhrmeister B., Wolter U., Schmitt J. H. M. M., Engels D., Wieringa M. H., 2013, A&A, 560, A69

Laming J. M., 2004, ApJ, 614, 1063

Laming J. M., 2015, Living Rev. Sol. Phys., 12, 2

Laming J. M., 2021, ApJ, 909, 17

Laming J. M., Drake J. J., Widing K. G., 1995, ApJ, 443, 416

Liefke C., Ness J. U., Schmitt J. H. M. M., Maggio A., 2008, A&A, 491, 859

Maehara H. et al., 2012, Nature, 485, 478

Maggio A., Pallavicini R., Reale F., Tagliaferri G., 2000, A&A, 356, 627

Mason K. O. et al., 2001, A&A, 365, L36

Mullan D., 2009, in Physics of the Sun. Chapman and Hall/CRC, New York

Namekata K. et al., 2021, Nat. Astron., 6, 241

Osten R. A., Brown A., 1999, ApJ, 515, 746

Osten R. A., Drake S., Tueller J., Cummings J., Perri M., Moretti A., Covino S., 2007, ApJ, 654, 1052

Pakull M. W., 1981, A&A, 104, 33

Pallavicini R., Tagliaferri G., Stella L., 1990, A&A, 228, 403

Pandey J. C., Singh K. P., 2008, MNRAS, 387, 1627

Pandey J. C., Singh K. P., 2012, MNRAS, 419, 1219

Parker E. N., 1988, ApJ, 330, 474

Pillitteri I., Argiroffi C., Maggio A., Micela G., Benatti S., Reale F., Colombo S., Wolk S. J., 2022, A&A, 666, A198

Reale F., 2007, A&A, 471, 271

Reale F., 2014, Living Rev. Sol. Phys., 11, 4

Reale F., Betta R., Peres G., Serio S., McTiernan J., 1997, A&A, 325, 782

Rosner R., Tucker W. H., Vaiana G. S., 1978, ApJ, 220, 643

Sanz-Forcada J., Maggio A., Micela G., 2003, A&A, 408, 1087

Sanz-Forcada J., Favata F., Micela G., 2004, A&A, 416, 281

Schaefer B. E., King J. R., Deliyannis C. P., 2000, ApJ, 529, 1026

Serio S., Reale F., Jakimiec J., Sylwester B., Sylwester J., 1991, A&A, 241, 197

Shibayama T. et al., 2013, ApJS, 209, 5

Smith R. K., Brickhouse N. S., Liedahl D. A., Raymond J. C., 2001, ApJ, 556, L91

Stelzer B. et al., 2002, A&A, 392, 585

Stern R. A., Uchida Y., Tsuneta S., Nagase F., 1992, ApJ, 400, 321

Strüder L. et al., 2001, A&A, 365, L18

Sylwester B., Sylwester J., Serio S., Reale F., Bentley R. D., Fludra A., 1993, A&A, 267, 586

Telleschi A., Güdel M., Briggs K., Audard M., Ness J.-U., Skinner S. L., 2005, ApJ, 622, 653

Tsuboi Y. et al., 2016, PASJ, 68, 90

Tsuru T. et al., 1989, PASJ, 41, 679

Turner M. J. L. et al., 2001, A&A, 365, L27

van den Oord G. H. J., Mewe R., 1989, A&A, 213, 245

van den Oord G. H. J., Mewe R., Brinkman A. C., 1988, A&A, 205, 181

Veronig A. M., Odert P., Leitzinger M., Dissauer K., Fleck N. C., Hudson H. S., 2021, Nat. Astron., 5, 697

Vilhu O., Linsky J. L., 1987, PASP, 99, 1071

Vilhu O., Tsuru T., Collier Cameron A., Budding E., Banks T., Slee B., Ehrenfreund P., Foing B. H., 1993, A&A, 278, 467

von Steiger R., Schweingruber R. F. W., Geiss J., Gloeckler G., 1995, Adv. Space Res., 15, 3

Wood B. E., Linsky J. L., 2010, ApJ, 717, 1279

Wood B. E., Laming J. M., Karovska M., 2012, ApJ, 753, 76

Wood B. E., Laming J. M., Warren H. P., Poppenhaeger K., 2018, ApJ, 862, 66

Yan Y., He H., Li C., Esamdin A., Tan B. L., Zhang L. Y., Wang H., 2021, MNRAS, 505, L79

Yashiro S., Gopalswamy N., 2009, in Gopalswamy N., Webb D. F., eds, Universal Heliophysical Processes (Vol. 257). Cambridge Univ. Press, Cambridge, p. 233

Zimovets I. V., Sharykin I. N., Gan W. Q., 2020, ApJ, 891, 138

APPENDIX A: SPECTRAL EVOLUTION OF FLARES

Table A1. Best-fitting spectral parameters of each temporal segment of the flares F1-F10, F13, F15, and F20. Here, FS represents flare segments, and ST and ET refer to the start and end times, respectively of each flare segment relative to the start time of the corresponding observation.

Set	Flare	FS	ST:ET (ks)	kT_3 (keV)	EM_3 (10^{52} cm^{-3})	Z ($Z_\odot$)	L_{XF} (10^{30} erg s^{-1})	χ^2_ν (dof)
S1	F1	R	4.8 : 5.7	$3.8^{+0.2}_{-0.2}$	$5.4^{+0.2}_{-0.2}$	$0.193^{+0.004}_{-0.005}$	$1.71^{+0.01}_{-0.01}$	1.1 (352)
		P	5.7 : 6.3	$3.7^{+0.1}_{-0.1}$	$15.7^{+0.3}_{-0.3}$	$0.255^{+0.007}_{-0.007}$	$3.34^{+0.02}_{-0.02}$	1.54 (426)
		D1	6.3 : 6.9	$2.49^{+0.09}_{-0.1}$	$11.0^{+0.3}_{-0.3}$	$0.281^{+0.007}_{-0.007}$	$2.5^{+0.02}_{-0.02}$	1.33 (350)
		D2	6.9 : 7.4	$2.8^{+0.1}_{-0.1}$	$9.6^{+0.3}_{-0.3}$	$0.243^{+0.007}_{-0.007}$	$2.27^{+0.02}_{-0.02}$	1.03 (317)
	F2	R	7.4 : 8.2	$3.0^{+0.1}_{-0.1}$	$11.1^{+0.3}_{-0.3}$	$0.225^{+0.007}_{-0.007}$	$2.45^{+0.02}_{-0.02}$	1.05 (360)
		P	8.2 : 9.3	$2.56^{+0.09}_{-0.07}$	$11.9^{+0.2}_{-0.3}$	$0.248^{+0.006}_{-0.006}$	$2.52^{+0.01}_{-0.01}$	1.0 (432)
		D1	9.3 : 10.1	$2.37^{+0.07}_{-0.07}$	$10.2^{+0.3}_{-0.3}$	$0.246^{+0.006}_{-0.006}$	$2.28^{+0.01}_{-0.01}$	0.98 (374)
		D2	10.1 : 11.0	$2.35^{+0.08}_{-0.08}$	$7.9^{+0.2}_{-0.2}$	$0.232^{+0.005}_{-0.005}$	$1.97^{+0.01}_{-0.01}$	1.16 (365)
		D3	11.0 : 12.0	$2.38^{+0.1}_{-0.09}$	$6.2^{+0.2}_{-0.2}$	$0.206^{+0.005}_{-0.005}$	$1.7^{+0.01}_{-0.01}$	1.29 (350)
		D4	12.0 : 13.2	$2.6^{+0.1}_{-0.1}$	$4.7^{+0.2}_{-0.2}$	$0.209^{+0.004}_{-0.004}$	$1.56^{+0.01}_{-0.01}$	1.08 (359)
		D5	13.2 : 14.4	$2.3^{+0.1}_{-0.1}$	$4.3^{+0.2}_{-0.2}$	$0.185^{+0.004}_{-0.004}$	$1.42^{+0.01}_{-0.01}$	1.05 (343)
		D6	14.4 : 15.7	$2.5^{+0.2}_{-0.1}$	$3.9^{+0.2}_{-0.2}$	$0.181^{+0.004}_{-0.004}$	$1.38^{+0.01}_{-0.01}$	1.1 (349)
		D7	15.7 : 17.0	$2.6^{+0.2}_{-0.2}$	$2.8^{+0.2}_{-0.2}$	$0.174^{+0.004}_{-0.004}$	$1.24^{+0.01}_{-0.01}$	1.04 (330)
		D8	17.0 : 18.3	$2.6^{+0.2}_{-0.2}$	$2.2^{+0.1}_{-0.1}$	$0.174^{+0.003}_{-0.003}$	$1.17^{+0.01}_{-0.01}$	1.03 (336)
		D9	18.3 : 20.0	$2.5^{+0.2}_{-0.2}$	$1.9^{+0.1}_{-0.1}$	$0.169^{+0.003}_{-0.003}$	$1.12^{+0.01}_{-0.01}$	1.07 (328)
		D10	20.0 : 21.4	$3.0^{+0.4}_{-0.3}$	$1.3^{+0.1}_{-0.1}$	$0.167^{+0.003}_{-0.003}$	$1.05^{+0.01}_{-0.01}$	1.19 (310)
	F3	R	24.3 : 25.6	$2.9^{+0.2}_{-0.1}$	$4.2^{+0.2}_{-0.2}$	$0.173^{+0.004}_{-0.004}$	$1.41^{+0.01}_{-0.01}$	1.12 (358)
		P	25.6 : 27.2	$2.33^{+0.06}_{-0.08}$	$8.2^{+0.2}_{-0.2}$	$0.216^{+0.004}_{-0.004}$	$1.94^{+0.01}_{-0.01}$	1.35 (446)
		D1	27.2 : 28.8	$2.10^{+0.06}_{-0.06}$	$6.3^{+0.2}_{-0.2}$	$0.219^{+0.004}_{-0.004}$	$1.71^{+0.01}_{-0.01}$	1.26 (414)
		D2	28.8 : 30.6	$2.14^{+0.06}_{-0.06}$	$5.7^{+0.2}_{-0.2}$	$0.204^{+0.004}_{-0.004}$	$1.61^{+0.01}_{-0.01}$	1.14 (418)
		D3	30.6 : 32.6	$2.16^{+0.07}_{-0.06}$	$5.5^{+0.1}_{-0.1}$	$0.187^{+0.003}_{-0.003}$	$1.53^{+0.01}_{-0.01}$	1.2 (428)
		D4	32.6 : 34.3	$2.13^{+0.08}_{-0.07}$	$4.7^{+0.2}_{-0.2}$	$0.182^{+0.004}_{-0.004}$	$1.43^{+0.01}_{-0.01}$	1.0 (386)
		D5	34.3 : 36.4	$2.02^{+0.08}_{-0.07}$	$3.8^{+0.1}_{-0.1}$	$0.176^{+0.003}_{-0.003}$	$1.31^{+0.01}_{-0.01}$	1.02 (391)
S2	F4	R	4.1 : 5.1	$3.0^{+0.1}_{-0.1}$	$3.6^{+0.2}_{-0.2}$	$0.202^{+0.005}_{-0.005}$	$1.27^{+0.01}_{-0.01}$	1.28 (299)
		P	5.1 : 6.0	$2.15^{+0.1}_{-0.08}$	$5.4^{+0.2}_{-0.2}$	$0.228^{+0.006}_{-0.005}$	$1.54^{+0.01}_{-0.01}$	1.12 (334)
		D1	6.0 : 6.7	$1.89^{+0.1}_{-0.1}$	$3.7^{+0.2}_{-0.2}$	$0.224^{+0.006}_{-0.006}$	$1.33^{+0.01}_{-0.01}$	1.15 (281)
		D2	6.7 : 7.5	$1.93^{+0.1}_{-0.1}$	$3.2^{+0.2}_{-0.2}$	$0.217^{+0.005}_{-0.005}$	$1.26^{+0.01}_{-0.01}$	1.09 (287)
		D3	7.5 : 8.3	$1.86^{+0.1}_{-0.1}$	$2.9^{+0.2}_{-0.2}$	$0.208^{+0.005}_{-0.005}$	$1.21^{+0.01}_{-0.01}$	1.16 (281)
		D4	8.3 : 9.1	$2.15^{+0.2}_{-0.2}$	$2.6^{+0.2}_{-0.2}$	$0.203^{+0.005}_{-0.005}$	$1.18^{+0.01}_{-0.01}$	1.26 (279)
		D5	9.1 : 10.5	$1.73^{+0.1}_{-0.1}$	$2.2^{+0.2}_{-0.2}$	$0.2^{+0.005}_{-0.005}$	$1.11^{+0.01}_{-0.01}$	1.11 (276)
	F5	R1	10.5 : 11.7	$1.96^{+0.2}_{-0.1}$	$2.2^{+0.2}_{-0.2}$	$0.208^{+0.005}_{-0.005}$	$1.14^{+0.01}_{-0.01}$	1.03 (262)
		R2	11.7 : 12.4	$2.66^{+0.2}_{-0.2}$	$2.8^{+0.2}_{-0.2}$	$0.22^{+0.005}_{-0.005}$	$1.28^{+0.01}_{-0.01}$	1.08 (265)
		P	12.4 : 13.1	$2.14^{+0.2}_{-0.1}$	$3.2^{+0.2}_{-0.2}$	$0.231^{+0.006}_{-0.006}$	$1.32^{+0.01}_{-0.01}$	1.11 (264)
		D1	13.1 : 13.9	$1.93^{+0.1}_{-0.1}$	$3.1^{+0.2}_{-0.2}$	$0.211^{+0.006}_{-0.006}$	$1.24^{+0.01}_{-0.01}$	1.06 (275)
		D2	13.9 : 14.7	$1.78^{+0.1}_{-0.1}$	$2.8^{+0.2}_{-0.2}$	$0.209^{+0.006}_{-0.006}$	$1.2^{+0.01}_{-0.01}$	1.09 (267)
		D3	14.7 : 15.5	$1.93^{+0.1}_{-0.1}$	$2.1^{+0.2}_{-0.2}$	$0.21^{+0.005}_{-0.005}$	$1.14^{+0.01}_{-0.01}$	1.08 (259)
		D4	15.5 : 16.3	$1.86^{+0.2}_{-0.2}$	$1.7^{+0.2}_{-0.2}$	$0.209^{+0.005}_{-0.005}$	$1.09^{+0.01}_{-0.01}$	1.25 (251)
		D5	16.3 : 17.3	$1.82^{+0.2}_{-0.2}$	$0.9^{+0.2}_{-0.1}$	$0.205^{+0.004}_{-0.004}$	$1.0^{+0.01}_{-0.01}$	1.28 (259)
	F6	R	29.1 : 29.8	$3.6^{+0.26}_{-0.23}$	$4.7^{+0.2}_{-0.2}$	$0.198^{+0.005}_{-0.005}$	$1.51^{+0.01}_{-0.01}$	1.31 (301)
		P	29.8 : 30.2	$2.99^{+0.17}_{-0.15}$	$8.6^{+0.3}_{-0.3}$	$0.256^{+0.008}_{-0.007}$	$2.1^{+0.02}_{-0.02}$	1.17 (310)
		D1	30.2 : 30.6	$2.99^{+0.2}_{-0.17}$	$6.6^{+0.3}_{-0.3}$	$0.247^{+0.007}_{-0.007}$	$1.84^{+0.02}_{-0.02}$	1.11 (287)
		D2	30.6 : 31.1	$3.21^{+0.22}_{-0.19}$	$5.6^{+0.2}_{-0.2}$	$0.216^{+0.006}_{-0.006}$	$1.65^{+0.01}_{-0.01}$	0.97 (289)
		D3	31.1 : 31.6	$3.27^{+0.25}_{-0.22}$	$4.6^{+0.2}_{-0.2}$	$0.201^{+0.006}_{-0.006}$	$1.49^{+0.01}_{-0.01}$	0.97 (277)
		D4	31.6 : 32.6	$2.92^{+0.2}_{-0.19}$	$4.5^{+0.2}_{-0.2}$	$0.181^{+0.006}_{-0.006}$	$1.4^{+0.01}_{-0.01}$	1.05 (268)

Table A1 – *continued*

Set	Flare	FS	ST:ET (ks)	kT_3 (keV)	EM_3 (10^{52} cm^{-3})	Z (Z$_\odot$)	L_{XF} (10^{30} erg s^{-1})	χ^2_ν (dof)
	F7	R1	32.6 : 34.1	$3.08^{+0.1}_{-0.1}$	$6.8^{+0.2}_{-0.2}$	$0.194^{+0.004}_{-0.004}$	$1.74^{+0.01}_{-0.01}$	1.13 (434)
		R2	34.1 : 35.1	$2.98^{+0.08}_{-0.08}$	$11.6^{+0.2}_{-0.2}$	$0.202^{+0.005}_{-0.005}$	$2.35^{+0.01}_{-0.01}$	1.03 (453)
		P	35.1 : 36.2	$2.76^{+0.06}_{-0.06}$	$14.4^{+0.2}_{-0.2}$	$0.218^{+0.005}_{-0.005}$	$2.65^{+0.01}_{-0.01}$	1.21 (488)
		D1	36.2 : 37.6	$2.51^{+0.06}_{-0.05}$	$11.2^{+0.2}_{-0.2}$	$0.224^{+0.005}_{-0.005}$	$2.25^{+0.01}_{-0.01}$	1.26 (482)
		D2	37.6 : 39.2	$2.48^{+0.06}_{-0.06}$	$8.6^{+0.2}_{-0.2}$	$0.215^{+0.004}_{-0.004}$	$1.92^{+0.01}_{-0.01}$	1.01 (460)
		D3	39.2 : 42.0	$2.31^{+0.06}_{-0.06}$	$8.0^{+0.2}_{-0.2}$	$0.197^{+0.004}_{-0.004}$	$1.77^{+0.01}_{-0.01}$	1.1 (457)
	F8	R1	42.0 : 42.9	$2.26^{+0.1}_{-0.09}$	$6.9^{+0.2}_{-0.2}$	$0.226^{+0.006}_{-0.006}$	$1.73^{+0.01}_{-0.01}$	1.02 (327)
		R2	42.9 : 43.6	$2.6^{+0.1}_{-0.1}$	$8.6^{+0.3}_{-0.3}$	$0.249^{+0.007}_{-0.007}$	$2.02^{+0.01}_{-0.01}$	1.1 (342)
		R3	43.6 : 44.2	$2.5^{+0.1}_{-0.1}$	$10.0^{+0.3}_{-0.3}$	$0.244^{+0.007}_{-0.007}$	$2.18^{+0.02}_{-0.02}$	1.08 (332)
		R4	44.2 : 44.8	$2.8^{+0.1}_{-0.1}$	$12.5^{+0.3}_{-0.3}$	$0.219^{+0.007}_{-0.007}$	$2.48^{+0.02}_{-0.02}$	1.11 (360)
		R5	44.8 : 45.3	$3.0^{+0.1}_{-0.1}$	$16.88^{+0.4}_{-0.4}$	$0.215^{+0.008}_{-0.008}$	$3.04^{+0.02}_{-0.02}$	1.11 (376)
		P	45.3 : 45.8	$2.56^{+0.1}_{-0.07}$	$17.6^{+0.4}_{-0.5}$	$0.225^{+0.01}_{-0.009}$	$3.01^{+0.02}_{-0.02}$	1.17 (369)
		D	45.8 : 46.3	$2.42^{+0.09}_{-0.07}$	$17.4^{+0.4}_{-0.5}$	$0.257^{+0.01}_{-0.009}$	$3.04^{+0.02}_{-0.02}$	0.95 (368)
	F9	R1	46.3 : 46.7	$2.46^{+0.08}_{-0.09}$	$17.4^{+0.5}_{-0.4}$	$0.29^{+0.01}_{-0.01}$	$3.17^{+0.02}_{-0.02}$	1.0 (339)
		R2	46.7 : 47.1	$2.47^{+0.07}_{-0.08}$	$20.3^{+0.5}_{-0.5}$	$0.27^{+0.01}_{-0.01}$	$3.46^{+0.03}_{-0.03}$	1.03 (356)
		R3	47.1 : 47.4	$2.71^{+0.09}_{-0.08}$	$20.1^{+0.5}_{-0.5}$	$0.32^{+0.01}_{-0.01}$	$3.72^{+0.03}_{-0.03}$	1.24 (371)
		P	47.4 : 47.8	$2.54^{+0.07}_{-0.07}$	$20.5^{+0.5}_{-0.5}$	$0.32^{+0.01}_{-0.01}$	$3.69^{+0.03}_{-0.03}$	0.92 (366)
		D	47.8 : 48.2	$2.22^{+0.06}_{-0.06}$	$19.3^{+0.5}_{-0.5}$	$0.31^{+0.01}_{-0.01}$	$3.39^{+0.02}_{-0.02}$	1.04 (355)
S3	F10	R	39.04 : 40.49	$3.5^{+0.3}_{-0.3}$	$6.8^{+0.4}_{-0.4}$	$0.25^{+0.01}_{-0.01}$	$1.87^{+0.02}_{-0.02}$	0.88 (208)
		P	40.49 : 40.94	$3.2^{+0.2}_{-0.2}$	$16.7^{+0.7}_{-0.7}$	$0.25^{+0.02}_{-0.02}$	$3.15^{+0.04}_{-0.04}$	1.02 (230)
		D1	40.94 : 41.49	$2.5^{+0.2}_{-0.2}$	$11.2^{+0.5}_{-0.5}$	$0.28^{+0.01}_{-0.01}$	$2.34^{+0.03}_{-0.03}$	1.14 (252)
		D2	41.49 : 42.19	$2.1^{+0.1}_{-0.1}$	$7.6^{+0.4}_{-0.4}$	$0.23^{+0.01}_{-0.01}$	$1.73^{+0.02}_{-0.02}$	1.09 (228)
		D3	42.19 : 43.04	$1.8^{+0.2}_{-0.1}$	$4.8^{+0.4}_{-0.4}$	$0.23^{+0.01}_{-0.01}$	$1.39^{+0.02}_{-0.02}$	0.94 (216)
S4	F13	P	37.63 : 38.23	$2.9^{+0.1}_{-0.1}$	$14.6^{+0.5}_{-0.5}$	$0.33^{+0.02}_{-0.02}$	$2.68^{+0.03}_{-0.03}$	0.97 (268)
		D1	38.23 : 38.63	$2.6^{+0.1}_{-0.1}$	$10.5^{+0.4}_{-0.3}$	$0.33^{+0.01}_{-0.01}$	$2.11^{+0.02}_{-0.02}$	1.15 (272)
		D2	38.63 : 39.13	$2.07^{+0.08}_{-0.1}$	$9.1^{+0.4}_{-0.3}$	$0.28^{+0.01}_{-0.01}$	$1.72^{+0.02}_{-0.02}$	1.08 (270)
		D3	39.13 :39.63	$1.67^{+0.07}_{-0.08}$	$6.7^{+0.3}_{-0.3}$	$0.28^{+0.01}_{-0.01}$	$1.4^{+0.02}_{-0.02}$	1.24 (240)
		D4	39.63 :40.23	$1.57^{+0.05}_{-0.06}$	$5.6^{+0.3}_{-0.2}$	$0.29^{+0.01}_{-0.01}$	$1.31^{+0.01}_{-0.01}$	1.14 (244)
S5	F15	R1	8.19 : 9.39	$5.7^{+0.3}_{-0.3}$	$30.0^{+0.6}_{-0.6}$	$0.29^{+0.01}_{-0.01}$	$6.40^{+0.05}_{-0.05}$	1.03 (411)
		R2	9.39 : 9.59	$7.4^{+0.3}_{-0.3}$	199^{+3}_{-3}	$0.50^{+0.04}_{-0.04}$	$38.9^{+0.3}_{-0.3}$	1.09 (561)
		R3	9.59 : 9.69	$7.7^{+0.4}_{-0.3}$	315^{+5}_{-5}	$0.53^{+0.06}_{-0.06}$	$61.5^{+0.4}_{-0.4}$	1.14 (557)
		R4	9.69 : 9.79	$6.7^{+0.3}_{-0.2}$	405^{+7}_{-7}	$0.41^{+0.06}_{-0.05}$	$73.7^{+0.6}_{-0.6}$	1.21 (472)
		R5	9.79 : 9.99	$5.8^{+0.2}_{-0.2}$	461^{+7}_{-7}	$0.40^{+0.04}_{-0.04}$	$81.0^{+0.6}_{-0.6}$	1.06 (532)
		R6	9.99 : 10.09	$5.3^{+0.2}_{-0.2}$	450^{+9}_{-9}	$0.54^{+0.06}_{-0.06}$	$80.6^{+0.7}_{-0.7}$	1.12 (432)
		P	10.09 : 10.19	$4.8^{+0.2}_{-0.1}$	491^{+9}_{-9}	$0.42^{+0.05}_{-0.05}$	$81.9^{+0.7}_{-0.7}$	1.15 (451)
S6	*F20	R	68.0 : 70.2	$2.7^{+0.3}_{-0.2}$	$47.2^{+0.6}_{-0.5}$	**	$4.80^{+0.04}_{-0.04}$	1.28 (657)
		P	70.2 : 71.5	$2.07^{+0.05}_{-0.08}$	132^{+1}_{-1}	**	$12.19^{+0.08}_{-0.09}$	1.35 (906)
		D1	71.5 : 73.3	$1.97^{+0.03}_{-0.03}$	$92.4^{+0.7}_{-0.7}$	**	$8.84^{+0.06}_{-0.06}$	1.76 (925)
		D2	73.3 : 76.2	$1.79^{+0.02}_{-0.02}$	$55.1^{+0.5}_{-0.5}$	**	$5.57^{+0.04}_{-0.04}$	1.95 (962)
		D3	76.2 : 81.1	$1.68^{+0.03}_{-0.03}$	$27.8^{+0.3}_{-0.3}$	**	$3.16^{+0.02}_{-0.02}$	1.90 (947)
		D4	81.1 : 90.3	$1.65^{+0.03}_{-0.06}$	$10.7^{+0.1}_{-0.1}$	**	$1.62^{+0.01}_{-0.01}$	1.62 (948)

*Spectral fitting was carried out using RGS spectra.
**The abundances were fixed to the quiescent state values of segment P11.

Table A2. Best-fitting spectral parameters as obtained from the spectral fitting of RGS spectra. All the parameters are quoted with a 68 per cent confidence interval.

Segments ($\downarrow$)	T_1 (keV)	T_2 (keV)	T_3 (keV)	EM_1 (10^{52} cm^{-3})	EM_2 (10^{52} cm^{-3})	EM_3 (10^{52} cm^{-3})	C	N	O	Ne	Mg	Si	S	Ar	Fe	L_{XF} (10^{30} erg s^{-1})	χ^2_ν (dof)
S2-P3	$0.28^{+0.01}_{-0.01}$	$0.76^{+0.03}_{-0.02}$	$1.7^{+0.2}_{-0.2}$	$1.9^{+0.2}_{-0.2}$	$4.2^{+0.4}_{-0.4}$	$3.9^{+0.3}_{-0.3}$	$0.7^{+0.1}_{-0.1}$	$0.7^{+0.1}_{-0.1}$	$0.37^{+0.04}_{-0.04}$	$1.2^{+0.1}_{-0.1}$	$0.22^{+0.08}_{-0.08}$	$0.3^{+0.1}_{-0.1}$	$0.2^{+0.1}_{-0.1}$	$0.9^{+0.3}_{-0.3}$	$0.17^{+0.02}_{-0.02}$	$1.07^{+0.01}_{-0.01}$	1.31 (434)
F4	–	–	$1.66^{+0.1}_{-0.08}$	–	–	$4.1^{+0.2}_{-0.2}$	$0.87^{+0.09}_{-0.09}$	$0.73^{+0.09}_{-0.09}$	$0.39^{+0.01}_{-0.01}$	$1.39^{+0.08}_{-0.08}$	$0.32^{+0.07}_{-0.07}$	$0.3^{+0.1}_{-0.1}$	$0.5^{+0.1}_{-0.1}$	$0.7^{+0.2}_{-0.2}$	$0.182^{+0.006}_{-0.006}$	$1.14^{+0.01}_{-0.01}$	1.34 (583)
F5	–	–	$1.8^{+0.2}_{-0.1}$	–	–	$2.7^{+0.2}_{-0.1}$	$0.81^{+0.07}_{-0.07}$	$0.49^{+0.06}_{-0.06}$	$0.39^{+0.01}_{-0.01}$	$1.29^{+0.06}_{-0.06}$	$0.29^{+0.06}_{-0.06}$	$0.27^{+0.07}_{-0.07}$	$0.34^{+0.07}_{-0.07}$	$0.8^{+0.1}_{-0.1}$	$0.175^{+0.004}_{-0.004}$	$0.973^{+0.007}_{-0.007}$	1.60 (811)
P4	$0.30^{+0.01}_{-0.02}$	$0.73^{+0.02}_{-0.03}$	$1.8^{+0.4}_{-0.3}$	$1.6^{+0.2}_{-0.2}$	$3.1^{+0.4}_{-0.3}$	$2.1^{+0.2}_{-0.2}$	$0.9^{+0.2}_{-0.2}$	$0.7^{+0.1}_{-0.1}$	$0.45^{+0.04}_{-0.04}$	$1.5^{+0.2}_{-0.1}$	$0.37^{+0.08}_{-0.08}$	$0.8^{+0.2}_{-0.2}$	$0.6^{+0.2}_{-0.1}$	$1.1^{+0.3}_{-0.3}$	$0.19^{+0.02}_{-0.02}$	$0.811^{+0.008}_{-0.008}$	1.31 (471)
F6	–	–	$1.9^{+0.2}_{-0.1}$	–	–	$6.3^{+0.3}_{-0.3}$	$0.9^{+0.1}_{-0.1}$	$0.6^{+0.1}_{-0.1}$	$0.35^{+0.02}_{-0.02}$	$1.2^{+0.1}_{-0.1}$	$0.6^{+0.1}_{-0.1}$	$0.8^{+0.2}_{-0.2}$	$0.6^{+0.2}_{-0.2}$	$0.9^{+0.3}_{-0.3}$	$0.199^{+0.008}_{-0.008}$	$1.38^{+0.02}_{-0.02}$	1.14 (348)
F7	–	–	$1.94^{+0.09}_{-0.07}$	–	–	$10.2^{+0.2}_{-0.2}$	$0.75^{+0.07}_{-0.07}$	$0.64^{+0.07}_{-0.07}$	$0.35^{+0.01}_{-0.01}$	$1.16^{+0.06}_{-0.06}$	$0.24^{+0.06}_{-0.06}$	$0.45^{+0.09}_{-0.09}$	$0.11^{+0.08}_{-0.08}$	$1.1^{+0.1}_{-0.1}$	$0.180^{+0.005}_{-0.005}$	$1.65^{+0.01}_{-0.01}$	1.19 (1041)
F8	–	–	$1.92^{+0.09}_{-0.06}$	–	–	$15.0^{+0.3}_{-0.3}$	$0.89^{+0.09}_{-0.09}$	$0.7^{+0.1}_{-0.1}$	$0.41^{+0.01}_{-0.01}$	$1.30^{+0.08}_{-0.08}$	$0.30^{+0.07}_{-0.07}$	$0.6^{+0.1}_{-0.1}$	$0.4^{+0.1}_{-0.1}$	$1.1^{+0.2}_{-0.2}$	$0.220^{+0.007}_{-0.007}$	$2.25^{+0.01}_{-0.01}$	1.20 (971)
F9	–	–	$1.87^{+0.1}_{-0.09}$	–	–	$19.9^{+0.6}_{-0.6}$	$1.1^{+0.2}_{-0.2}$	$0.6^{+0.2}_{-0.2}$	$0.41^{+0.02}_{-0.02}$	$1.2^{+0.1}_{-0.1}$	$0.3^{+0.1}_{-0.1}$	$0.5^{+0.2}_{-0.2}$	$0.3^{+0.2}_{-0.2}$	$1.5^{+0.4}_{-0.4}$	$0.27^{+0.01}_{-0.01}$	$2.81^{+0.03}_{-0.03}$	1.19 (425)
S3-P5	$0.294^{+0.004}_{-0.004}$	$0.75^{+0.01}_{-0.01}$	$1.61^{+0.05}_{-0.03}$	$1.94^{+0.09}_{-0.08}$	$3.6^{+0.1}_{-0.1}$	$4.4^{+0.1}_{-0.1}$	$0.77^{+0.05}_{-0.05}$	$0.59^{+0.05}_{-0.04}$	$0.39^{+0.01}_{-0.01}$	$1.14^{+0.04}_{-0.04}$	$0.34^{+0.03}_{-0.03}$	$0.39^{+0.04}_{-0.04}$	$0.37^{+0.05}_{-0.05}$	$0.70^{+0.09}_{-0.09}$	$0.205^{+0.008}_{-0.007}$	$1.105^{+0.004}_{-0.004}$	1.46 (1923)
F10	–	–	$1.7^{+0.2}_{-0.1}$	–	–	$9.0^{+0.4}_{-0.4}$	$0.8^{+0.2}_{-0.2}$	$0.3^{+0.1}_{-0.1}$	$0.44^{+0.03}_{-0.03}$	$1.2^{+0.1}_{-0.1}$	$0.3^{+0.1}_{-0.1}$	$0.3^{+0.2}_{-0.2}$	$1.0^{+0.3}_{-0.3}$	$1.5^{+0.5}_{-0.5}$	$0.161^{+0.008}_{-0.008}$	$1.58^{+0.02}_{-0.02}$	1.18 (363)
S4-F11	–	–	$1.75^{+0.07}_{-0.09}$	–	–	$8.7^{+0.2}_{-0.2}$	$0.9^{+0.1}_{-0.1}$	$0.7^{+0.1}_{-0.1}$	$0.48^{+0.02}_{-0.02}$	$1.20^{+0.08}_{-0.09}$	$0.29^{+0.07}_{-0.07}$	$0.4^{+0.1}_{-0.1}$	$0.6^{+0.2}_{-0.2}$	$1.4^{+0.3}_{-0.3}$	$0.206^{+0.006}_{-0.006}$	$1.51^{+0.01}_{-0.01}$	1.12 (707)
P6	$0.28^{+0.01}_{-0.01}$	$0.70^{+0.01}_{-0.01}$	$1.68^{+0.09}_{-0.06}$	$1.5^{+0.1}_{-0.1}$	$3.8^{+0.2}_{-0.2}$	$5.1^{+0.2}_{-0.2}$	$0.86^{+0.09}_{-0.09}$	$0.59^{+0.07}_{-0.07}$	$0.44^{+0.02}_{-0.02}$	$1.20^{+0.07}_{-0.07}$	$0.36^{+0.05}_{-0.05}$	$0.32^{+0.07}_{-0.07}$	$0.5^{+0.1}_{-0.1}$	$1.2^{+0.2}_{-0.2}$	$0.17^{+0.01}_{-0.01}$	$1.134^{+0.007}_{-0.007}$	1.14 (1111)
F12	–	–	$1.69^{+0.09}_{-0.05}$	–	–	$8.9^{+0.2}_{-0.2}$	$0.6^{+0.1}_{-0.1}$	$0.9^{+0.1}_{-0.1}$	$0.47^{+0.02}_{-0.02}$	$1.36^{+0.08}_{-0.08}$	$0.33^{+0.07}_{-0.07}$	$0.4^{+0.1}_{-0.1}$	$0.5^{+0.1}_{-0.1}$	$1.1^{+0.3}_{-0.3}$	$0.209^{+0.006}_{-0.006}$	$1.54^{+0.01}_{-0.01}$	1.09 (717)
F13	–	–	$2.1^{+0.2}_{-0.2}$	–	–	$11.1^{+0.4}_{-0.4}$	$1.1^{+0.2}_{-0.2}$	$0.6^{+0.2}_{-0.2}$	$0.49^{+0.03}_{-0.03}$	$1.4^{+0.1}_{-0.1}$	$0.3^{+0.1}_{-0.1}$	$0.50^{+0.2}_{-0.2}$	$0.7^{+0.3}_{-0.3}$	$0.6^{+0.5}_{-0.5}$	$0.200^{+0.009}_{-0.009}$	$1.75^{+0.02}_{-0.02}$	1.12 (405)
P7	$0.29^{+0.01}_{-0.01}$	$0.70^{+0.02}_{-0.02}$	$1.59^{+0.1}_{-0.09}$	$1.3^{+0.2}_{-0.2}$	$3.8^{+0.3}_{-0.3}$	$4.6^{+0.3}_{-0.3}$	$1.1^{+0.2}_{-0.1}$	$0.6^{+0.1}_{-0.1}$	$0.47^{+0.04}_{-0.04}$	$1.4^{+0.1}_{-0.1}$	$0.24^{+0.07}_{-0.07}$	$0.6^{+0.1}_{-0.1}$	$0.4^{+0.2}_{-0.2}$	$1.3^{+0.4}_{-0.3}$	$0.17^{+0.02}_{-0.02}$	$1.10^{+0.01}_{-0.01}$	1.24 (510)
F14	–	–	$1.69^{+0.09}_{-0.05}$	–	–	$6.3^{+0.2}_{-0.2}$	$1.0^{+0.1}_{-0.1}$	$0.78^{+0.09}_{-0.09}$	$0.49^{+0.01}_{-0.01}$	$1.42^{+0.07}_{-0.07}$	$0.34^{+0.06}_{-0.06}$	$0.37^{+0.08}_{-0.08}$	$1.0^{+0.1}_{-0.1}$	$1.2^{+0.2}_{-0.2}$	$0.196^{+0.005}_{-0.005}$	$1.324^{+0.009}_{-0.009}$	1.13 (935)
S5-P8	$0.297^{+0.009}_{-0.01}$	$0.76^{+0.03}_{-0.02}$	$1.6^{+0.1}_{-0.1}$	$2.1^{+0.2}_{-0.2}$	$3.5^{+0.3}_{-0.2}$	$4.0^{+0.2}_{-0.2}$	$0.9^{+0.1}_{-0.1}$	$0.9^{+0.1}_{-0.1}$	$0.44^{+0.04}_{-0.03}$	$1.3^{+0.1}_{-0.1}$	$0.29^{+0.07}_{-0.07}$	$0.5^{+0.1}_{-0.1}$	$0.8^{+0.2}_{-0.2}$	$0.6^{+0.2}_{-0.2}$	$0.22^{+0.02}_{-0.02}$	$1.134^{+0.007}_{-0.007}$	1.22 (596)
F15	–	–	$4.94^{+0.07}_{-0.07}$	–	–	$120.6^{+0.7}_{-0.7}$	$2.4^{+0.1}_{-0.1}$	$1.6^{+0.1}_{-0.1}$	$1.12^{+0.02}_{-0.02}$	$3.00^{+0.08}_{-0.08}$	$0.72^{+0.09}_{-0.09}$	$0.7^{+0.1}_{-0.1}$	$2.7^{+0.2}_{-0.2}$	$3.4^{+0.4}_{-0.4}$	$0.90^{+0.01}_{-0.01}$	$15.05^{+0.03}_{-0.03}$	1.59 (3111)
F16	–	–	$1.91^{+0.1}_{-0.08}$	–	–	$12.5^{+0.6}_{-0.5}$	$1.7^{+0.4}_{-0.3}$	$1.3^{+0.3}_{-0.3}$	$0.96^{+0.05}_{-0.05}$	$2.6^{+0.2}_{-0.2}$	$0.6^{+0.2}_{-0.1}$	$0.6^{+0.2}_{-0.2}$	$0.7^{+0.4}_{-0.4}$	$1.5^{+0.7}_{-0.6}$	$0.44^{+0.02}_{-0.02}$	$2.51^{+0.03}_{-0.03}$	1.13 (3110)
P9	$0.294^{+0.004}_{-0.004}$	$0.74^{+0.01}_{-0.01}$	$1.69^{+0.04}_{-0.03}$	$1.53^{+0.06}_{-0.06}$	$3.23^{+0.09}_{-0.09}$	$4.72^{+0.08}_{-0.08}$	$0.86^{+0.05}_{-0.05}$	$0.70^{+0.04}_{-0.04}$	$0.45^{+0.01}_{-0.01}$	$1.38^{+0.04}_{-0.04}$	$0.38^{+0.03}_{-0.03}$	$0.31^{+0.04}_{-0.04}$	$0.49^{+0.05}_{-0.05}$	$0.81^{+0.09}_{-0.09}$	$0.202^{+0.006}_{-0.006}$	$1.10^{+0.01}_{-0.01}$	1.39 (2282)
S6-F17	–	–	$1.71^{+0.09}_{-0.08}$	–	–	$5.5^{+0.2}_{-0.2}$	$1.4^{+0.2}_{-0.2}$	$0.8^{+0.1}_{-0.1}$	$0.54^{+0.02}_{-0.02}$	$1.28^{+0.09}_{-0.09}$	$0.40^{+0.08}_{-0.08}$	$0.4^{+0.1}_{-0.1}$	$0.6^{+0.2}_{-0.2}$	$0.8^{+0.3}_{-0.3}$	$0.208^{+0.007}_{-0.007}$	$1.20^{+0.01}_{-0.01}$	1.19 (531)
F18	–	–	$1.88^{+0.08}_{-0.08}$	–	–	$6.6^{+0.2}_{-0.2}$	$1.3^{+0.2}_{-0.1}$	$0.7^{+0.1}_{-0.1}$	$0.53^{+0.02}_{-0.02}$	$1.25^{+0.07}_{-0.07}$	$0.29^{+0.07}_{-0.07}$	$0.5^{+0.1}_{-0.1}$	$0.4^{+0.1}_{-0.1}$	$0.9^{+0.2}_{-0.2}$	$0.213^{+0.006}_{-0.006}$	$1.29^{+0.01}_{-0.01}$	1.11 (822)
P11	$0.302^{+0.02}_{-0.008}$	$0.76^{+0.03}_{-0.01}$	$2.3^{+0.3}_{-0.2}$	$1.5^{+0.2}_{-0.1}$	$3.0^{+0.2}_{-0.2}$	$3.4^{+0.2}_{-0.2}$	$1.1^{+0.2}_{-0.2}$	$0.7^{+0.1}_{-0.1}$	$0.53^{+0.04}_{-0.03}$	$1.6^{+0.1}_{-0.1}$	$0.31^{+0.07}_{-0.07}$	$0.3^{+0.1}_{-0.1}$	$0.6^{+0.1}_{-0.1}$	$0.5^{+0.2}_{-0.2}$	$0.19^{+0.01}_{-0.01}$	$0.962^{+0.005}_{-0.005}$	1.18 (749)
F19	–	–	$1.79^{+0.1}_{-0.07}$	–	–	$8.8^{+0.3}_{-0.3}$	$0.9^{+0.2}_{-0.2}$	$0.8^{+0.2}_{-0.2}$	$0.46^{+0.02}_{-0.02}$	$1.3^{+0.1}_{-0.1}$	$0.5^{+0.1}_{-0.1}$	$0.6^{+0.1}_{-0.1}$	$0.8^{+0.2}_{-0.2}$	$0.5^{+0.3}_{-0.3}$	$0.250^{+0.009}_{-0.009}$	$1.6^{+0.01}_{-0.01}$	0.95 (509)
F20	–	–	$2.78^{+0.05}_{-0.05}$	–	–	$32.4^{+0.2}_{-0.2}$	$1.3^{+0.1}_{-0.1}$	$0.93^{+0.08}_{-0.08}$	$0.72^{+0.01}_{-0.01}$	$2.13^{+0.06}_{-0.06}$	$0.50^{+0.09}_{-0.08}$	$0.51^{+0.08}_{-0.1}$	$1.0^{+0.1}_{-0.1}$	$1.4^{+0.2}_{-0.2}$	$0.457^{+0.007}_{-0.006}$	$4.32^{+0.01}_{-0.01}$	1.42 (2440)
F21	–	–	$1.9^{+0.1}_{-0.1}$	–	–	$7.0^{+0.2}_{-0.2}$	$1.2^{+0.2}_{-0.2}$	$0.7^{+0.1}_{-0.1}$	$0.61^{+0.02}_{-0.02}$	$1.59^{+0.09}_{-0.09}$	$0.45^{+0.09}_{-0.08}$	$0.6^{+0.1}_{-0.1}$	$0.4^{+0.2}_{-0.2}$	$0.7^{+0.3}_{-0.3}$	$0.251^{+0.007}_{-0.007}$	$1.44^{+0.01}_{-0.01}$	1.21 (682)

This paper has been typeset from a TeX/LaTeX file prepared by the author.